Simulation-based optimisation of a Linear Fresnel Collector mirror field and receiver for optical, thermal and economic performance

M.A. Moghimi[**], K.J. Craig[*] and J.P. Meyer

Department of Mechanical and Aeronautical Engineering, University of Pretoria, Pretoria 0002, South Africa.

*Corresponding author: ken.craig@up.ac.za

** mohammad.moghimiardekani@up.ac.za, moghimi64@gmail.com

Abstract

Increasing the efficiency of concentrating solar power (CSP) technologies by means of optimisation tools is one of the current topics of solar thermal researchers. Of these technologies, Linear Fresnel collectors (LFCs) are the least developed. Therefore, there is plenty of room for the optimisation of this technology. One of the goals of this paper, in addition to the optimisation of an LFC plant, is introducing an applicable optimisation procedure that can be applied for any type of CSP plant. This paper focuses on harvesting maximum solar energy (maximising plant optical efficiency), as well as minimising plant thermal heat loss (maximising plant thermal efficiency), and plant cost (the economic optimisation of the plant), which leads to the generation of cheaper solar electricity from an LFC plant with a fixed power plant cycle (The performance optimisation of this study is based on the plant performance throughout an imaginary summer day). A multi-tube cavity receiver is considered in this study since there is plenty of room for its optimization. For the receiver, optimal cavity shape, tube bundle arrangement, tube numbers, cavity mounting height and insulation thickness are considered, while for the mirror field, the number of mirrors, mirror width, mirror gaps and mirror focal length are considered to achieve the optimisation goals. A multi-stage optimisation process is followed. Firstly, optical (using SolTrace), thermal (using a view area approach) and economic performance are combined in a multi-objective genetic algorithm as incorporated in ANSYS DesignXplorer (DX). This leads to an optimal LFC with a variable focal length for each mirror. After determining a fixed optimal focal length for all the mirrors, a Computational Fluid Dynamics (CFD) approach is used to optimise the thermal insulation of the cavity receiver for minimal heat loss and minimal insulation material. The process is automated through the use of ANSYS Workbench and Excel (coding with Visual Basic for Application (VBA) and LK Scripting in SolTrace). The view area approach provides an inexpensive way of calculating radiation heat loss from the receiver that is shown in the subsequent CFD analysis to be dominating the heat transfer loss mechanisms. The optimised receiver is evaluated at different LFC plant tube temperatures to assess its performance.

Keywords: Linear Fresnel Collector (LFC), Concentrating Solar Power (CSP), optimisation, optical, thermal, economic, Computational Fluid Dynamics (CFD), ray tracing.

1. Introduction

Global crises were the main drivers in moving human energy sources towards renewable sources and solar energy. For example, the oil and energy crisis of 1973 to 1979 (Ross, 2016) led to grants for scientific work to find a reliable alternative source of energy. Due to the funded scientific works in this period, the successful constructions of Concentration Solar Power (CSP) plants were begun. Examples of such plants are Solar One (Solar One, 2016), constructed in 1982 and operated until 1988, and the nine plants of Solar Energy Generation Systems (SEGS) (SEGS, 2016), constructed from 1984 to 1990 with a combined capacity of 354 MW. The dusk of this period started with the ending of the oil crisis. This period of crisis, however, helped CSP technologies prove themselves to be reliable eco-friendly sources of solar energy. Four main CSP technologies were introduced in this period: the Heliostat Field Collector (HFC), the Parabolic Dish Reflector (PDR), the Parabolic Trough Collector (PTC) and the Linear Fresnel Collector (LFC), although the research and development of these technologies did not take place at the same pace during this period. For instance, by the late 1980s, while great investment had been made into PTC plants, scientific research on LFC developments had only just begun and was halted at the end of the oil crisis and falling oil price. The second golden period of investment into CSP technologies was initiated by global warming in the 1990s and the Kyoto Protocol in 1997 (United Nations, 2016a) and was affected by the worldwide economic crises. The development of the LFC took place towards the end of this period. Despite the fact that the first LFC plant commissioned in Spain displayed its competitiveness with the PTC (Abbas et al., 2016), the Spanish government placed a moratorium on the construction of new renewable energy technologies that had not yet been approved (Government of Spain, 2012). This moratorium stopped the development of the LFC and signifies the end of the second period of CSP development. The third period of CSP development started with the help of US loan guarantees for different companies manufacturing CSP plants. This period mainly began because of energy dependence issues of the US government (Abbas et al., 2013). However, due to the achievements of the 21st Conference of the Parties (COP 21) to the United Nations Framework Convention on Climate Change (UNFCCC), which took place in Paris, France, in 2015 (United Nations, 2016b), the commitments and motivations of other countries to subsidise and move towards renewable energy have increased.

Although the LFC technology was developed late in the aforementioned periods, it proved its advantages in comparison with the most mature CSP plant technology (PTC) to name a few: easy maintenance, no requirement for high pressure joints, lower height of mirrors and lower wind loads, inexpensive mirror field and simple tracking system due to lightweight reflectors, and so on (consult Moghimi et al. (2015c) for a more detailed discussion). However, the disadvantages of LFC compared to PTC are higher optical losses (lower efficiency) and lower technology maturity (less reliability) which may lead to some difficulties in the financing conditions of such projects (Günther, 2017). Interesting investigations have taken place in the research and development of LFCs. Zhu et al. (2014) conducted a comprehensive study on the history of LFCs and presented promising LFC technologies. Among these technologies, two commercialised technologies received more attention by researchers. These are the LFC with a multi-tube cavity receiver (Singh et al., 1999; Sahoo et al., 2012; Abbas et al., 2013; Pye et al., 2003; Moghimi et al., 2014; Hongn et al., 2015) (see Fig. 1-b) and the

LFC with a mono-tube cavity receiver with a compound parabolic-shaped secondary reflector (Haberle et al., 2002; Heimsath et al., 2014; Sharma et al., 2015; Qiu et al., 2015; Moghimi et al. 2015a) (see Fig. 1-a). The first technology was commercialised by Areva Solar (Areva Solar, 2016) and the second by Novatech Solar (Novatech Solar, 2016) and Solarmundo (Zhu et al., 2014).

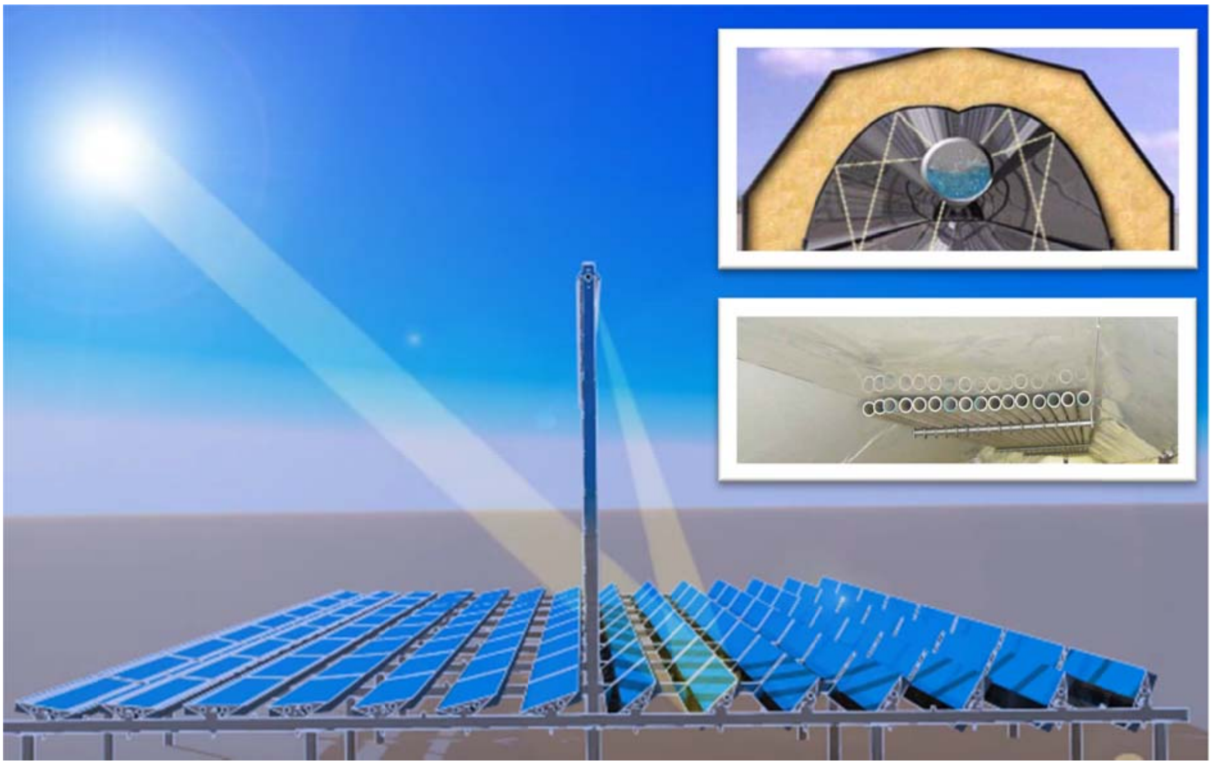

Fig. 1. Layout of LFC technology with the inserted images of cavity receiver configuration. Top right corner, mono-tube secondary reflector cavity receiver used in the Nova-1 project (Novatech Solar technology – reprinted from Selig and Mertins, 2010). Middle right side, multi-tube arrangement in a trapezoidal cavity during construction (reprinted from Pye, 2008).

The late development of LFC technologies left plenty of room for their optimisation and made them an interesting topic among researchers. However, due to the definition of a variety of optimisation objective goals, the results of those studies vary and hence do not provide a fixed utopian design. This issue will be addressed later when the results of a thermal and optical optimisation study are compared with an economic optimisation study on the same LFC configuration. Traditionally, researchers perform the economic optimisation of a CSP plant via the definition of Levelised Electricity Cost (LEC), also known as Levelised Cost of Electricity (LCOE) (LCOE, 2016) and its minimisation. The results of LEC minimisation may not predicate the same utopian design as a pure optical or thermal optimisation. For instance, Bernhard et al. (2008) reported on the results of an optimisation study of the FRESDEMO project which concerns an LFC plant with a mono-tube cavity receiver and secondary reflector. In that study, firstly, the receiver height, the tube diameter and the mirror width were determined based on practical restrictions. Then, the optimisation was performed on the set of independent parameters, consisting of the following: the number of mirrors, the mirror gaps, the mirror curvature, mirror aiming points and the shape of the secondary reflector. They reported that, for a constant field width, thermal efficiency reached its maximum value with 22 mirror rows, while the LEC optimisation of a similar problem showed that the minimum cost of the field occurred with 30 mirrors (Fig. 2). Indeed, adding more than 22 mirrors decreases the thermal efficiency because of the mirror shading and blocking effects in the constant field width, while mirror field cost decreases by increasing rows up to 30. In another study, Montes et al. (2012) conducted an optimisation study on the optical and thermal losses of the mirror field of the FRESDEMO plant disregarding economic factors of the plant and thermal and optical losses of cavity receiver. Their study's focus was on minimisation of shading and blocking, end and lateral losses, and mirror reflection losses of the FRESDEMO plant by changing the receiver height and mirror field total width parameters of the plant. These researchers showed that, for a constant receiver height, by increasing the mirror field width, annual energy efficiency (defined as incident energy in the receiver over the solar irradiation incident on the total mirror area) is boosted (Fig. 3-a), but that such a configuration (increasing mirror field width) increases the required material and land cost. Since a wider solar field decreases the shading and blocking annual ratios (Fig. 3-b) and more solar rays impinge on the absorber tube, annual harvested energy is boosted, while due to the installation of mirrors on a structure, a heavier and more expensive structure, as well as a greater land area, is required. Morin et al. (2006) performed LEC optimisation on the same configuration and found that there is an optimum mirror gap and that it is not economical at all to increase mirror gaps and consequently increase mirror field width as much as a designer would like to (Fig. 3-c). The same study can be repeated for an optimum economic mirror width.

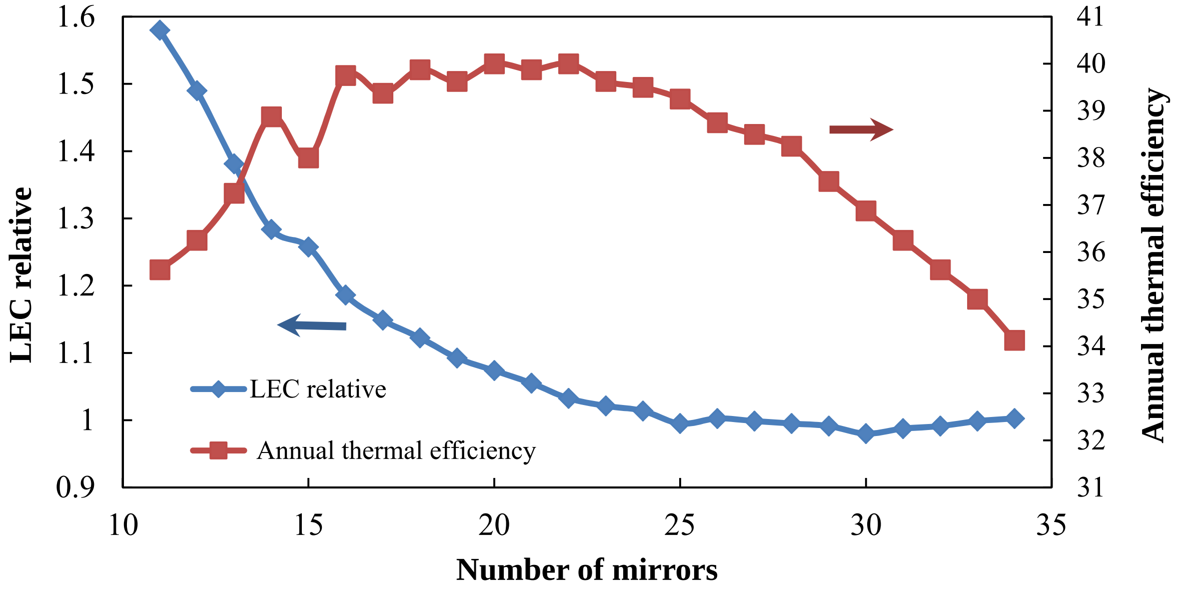

Fig. 2. The effect of the number of mirrors on annual thermal efficiency and relative LEC (data taken from Bernhard et al., 2008).

In terms of receiver elevation, Montes et al. (2012) and Morin et al. (2006) are among the researchers who tried to define optimum receiver height with or without considering economic factors. Whether economic factors are included (Fig. 3-d from Morin et al., 2006) or not (Fig. 3-a from Montes et al., 2012), optimum receiver height can lead to contrasting optimum designs. Note that the optimum height of around 8 to 10 m is specific to the setup studied by Morin et al., and not generally applicable. When the additional cost of the structure required to support a high receiver is excluded, a high receiver makes optical sense (Fig. 3-a), but when the cost is taken into consideration, there is a break-even point above which a higher reviver is penalised in terms of cost (Fig. 3-d).

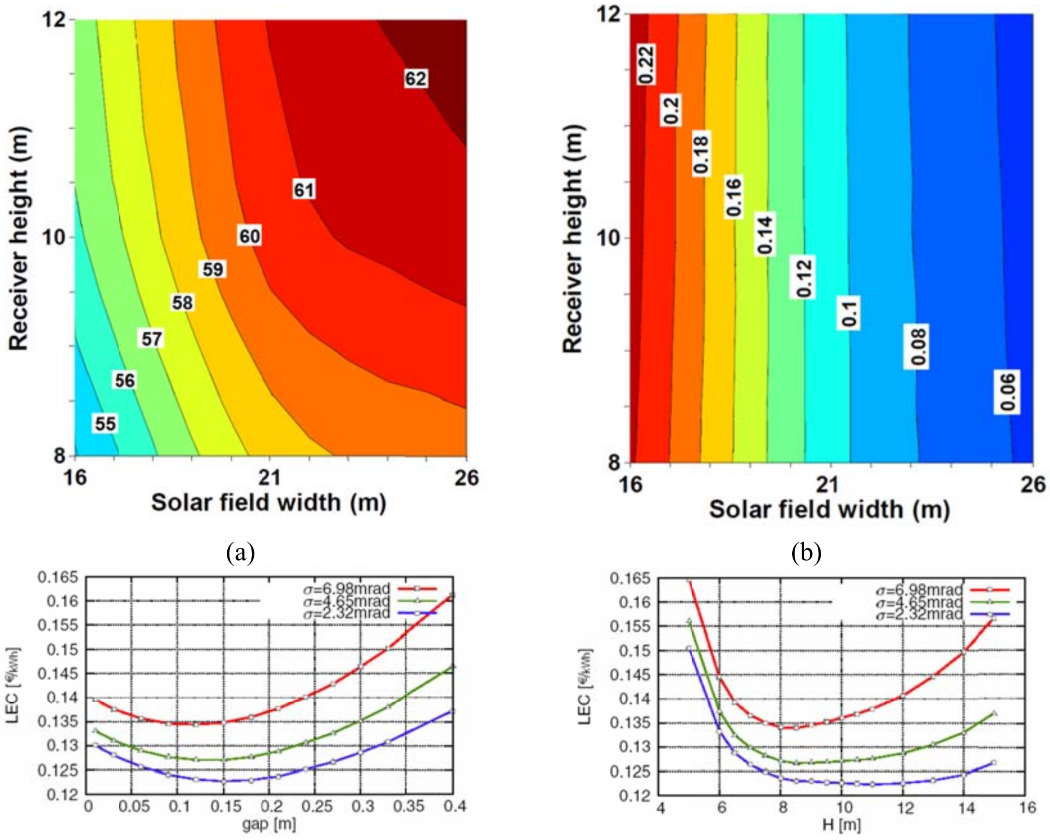

(a) (b)

(c) (d)

Fig. 3. The effects of different goals on optimisation outcomes of previous researchers. (a) 3D surface of Annual energy efficiency of an LFC vs. receiver height and solar field width displayed on a 2D plane (Montes et al., 2012). (b). 3D surface of the percentage annual shading of an LFC vs. receiver height and solar field width displayed on a 2D plane (Montes et al., 2012). (c) Effects of mirror gap on LEC (Morin et al., 2006). (d) Effects of receiver height on LEC (Morin et al., 2006).

With regard to receiver configuration, Mertins (2009) surveyed the economic optimisation of an LFC single-tube receiver. For instance, he studied the effect of two separate receiver tube diameters on the LEC, as well as the relative location of the tube receiver.

In summary, all the aforementioned economic optimisations were performed on a mono-tube receiver with a secondary reflector (Novatech Solar, 2016), while a similar comprehensive optimisation study for the trapezoidal multi-tube receiver (Areva solar, 2016) has not been conducted, which is the aim of the current paper.

This paper reports on a comprehensive optical, thermal and economic optimisation study conducted on an LFC field with a multi-tube cavity receiver with constant aperture width (Areva solar, 2016). The work reported here implements the suggested future work of Moghimi et al. (2015c) and tries to answer the questions faced by designers and researchers when designing an LFC with a multi-tube trapezoidal cavity receiver. These questions could include the following: What is the optimum number and width of mirrors, as these combined would define the total mirror area? What is the optimum gap between the mirrors? What is the optimum number of tubes in a tube bundle? What tube diameter should be considered for absorber tubes? What should the arrangement of tubes be? What is the optimum configuration trapezoidal cavity? What is the optimum mounting height of a cavity receiver? These questions may be encountered in the modelling and simulation of any other type of CSP plant. Therefore, by applying the described optimisation procedure in this paper on a chosen plant, these questions can be answered.

In order to maintain the accuracy of a comprehensive optimisation study of an LFC in a reasonable range, as well as to speed up the simulation, a two-stage optimisation process is suggested in this paper. In the first stage, all the collector domain parameters except insulation thickness are optimised. The second stage focuses on the insulation optimisation of the proposed utopian cavity in the first stage. The objectives of the first stage are obtained in by using Excel inside ANSYS WorkBench to drive SolTrace, while in the second stage, the optimisation objectives are determined in ANSYS FLUENT, again inside the WorkBench environment with parameterised models. By linking the corresponding software to ANSYS DesignXplorer (ANSYS DX), the optimisation loop for a corresponding problem is set.

This paper firstly presents the definition of the optimisation problem in the context of the collector layout, followed by a discussion of the engineering optimisation tools and modelling in three separate sections: economic modelling, thermal modelling and optical modelling. This is followed by the definition of the optimisation problems and optimisation algorithm settings. Finally, after discussing the optimisation and detailed Computational Fluid Dynamics (CFD) and ray-tracing results, conclusions are presented.

2. Definition of collector layout and engineering tools and modelling

2.1. Collector layout

An LFC is an array of slightly curved or flat mirrors that concentrate solar energy on a collection of absorber tube(s) surrounded by a downward-facing fixed receiver. In this study, a multi-tube trapezoidal cavity was considered as the LFC's receiver with the mirrors all having a slight parabolic curvature. The cavity is filled with air and the cavity aperture is covered by glass 3.2 mm thick to reduce radiative and convective heat losses from the cavity. Fig. 4 presents a schematic sketch of the proposed LFC. The aperture width is fixed at 332 mm to approximate the aperture condition of Solarmundo (Bernhard et al. (2008)), which was designed with a mono-tube secondary reflector cavity receiver. The aperture size selection essentially defines the system in terms of its ability to capture reflected solar energy. In order to determine an optimum LFC with these conditions, the other geometric parameters that are outlined later have to form a design variable set for the optimisation process. Those parameters, which are mostly shown in Fig. 4, are as follows: number of mirrors (N_m) and mirror width (W) (together defining total mirror area, which is a well-known terminology in this field), mirror gap (G- this term is defined based on the case when the mirrors are faced upward which mathematically is equivalent to mirror pitch (P) minus mirror width (W); G=P-W), mounting height of the cavity (H), cavity depth (*h*), location of the tube bundle in the cavity (*d*), number of tube absorbers (N_t), tube pitch (*m*), tube outer diameter (OD), cavity angle (θ), side and top insulation thicknesses (*b* and *t* - consult Fig. 8), and angle of top insulation (*d*- consult Fig. 8). In addition to these independent parameters, there are some dependent parameters that play a role in the optimisation process. These are determined by the mentioned design variable set. The slightly parabolic curvature of the mirrors is one such dependent parameter. The ideal parabola function for an LFC mirror's curvature is:

$$y = \frac{1}{4f} x^2 \tag{1}$$

where *f* is the distance in a 2-D plane from the mirror centre to the tube bundle centre (focal length). Therefore, as displayed in Fig. 4-a, the focal length of the j_{th} mirror is calculated as:

$$f_j = \sqrt{X_j^2 + Z^2} \tag{2}$$

where X_j is distance from the j_{th} mirror centre to the collector symmetry line (as influenced by the parameters: mirror gap, mirror width, and number of mirrors), and *Z* is the perpendicular tube bundle distance from the mirror field (determined mainly by the parameter: mounting height of the cavity, and to a lesser extent by the parameter: location of the tube bundle centre in the cavity).

Before performing the optimisation process, the available engineering tools and methods used in the calculation of the optimisation goals are surveyed.

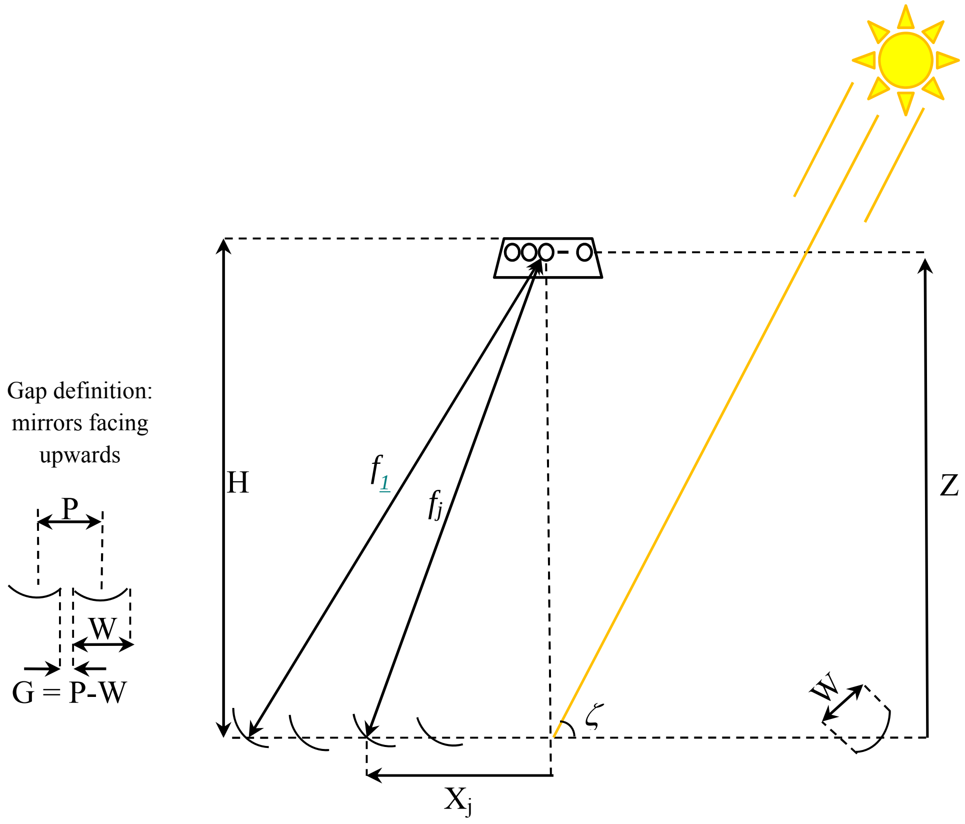

(a)

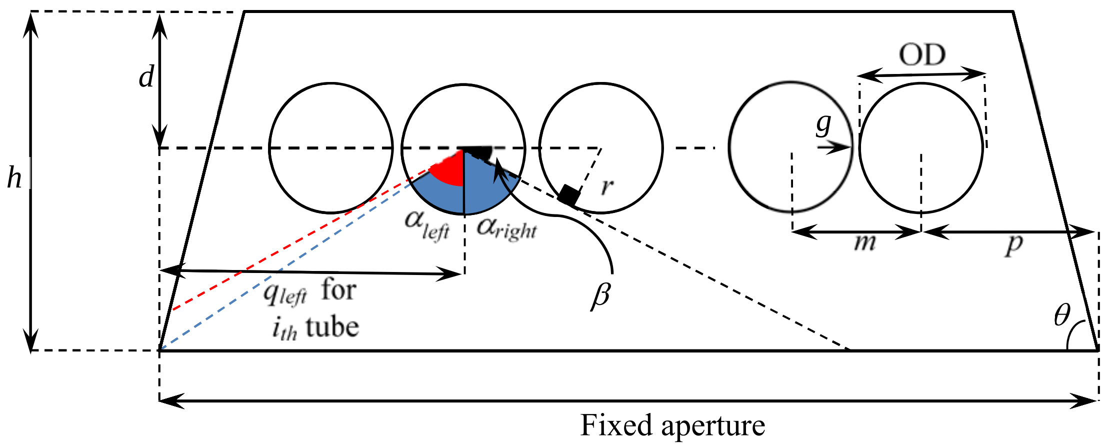

(b)

Fig. 4. Schematic sketch of an LFC. (a) Entire collector domain. (b) Cavity receiver.

2.2. *Optimisation tool*

The optimisation tool that was used in this study was ANSYS DX. The ANSYS platform allows researchers and designers to interact with Excel, commercial CFD codes, engineering tools and an optimisation tool (DX) in one integrated platform: WorkBench (WB). This makes the optimisation process more robust, customised, user-friendly and easier since the external interactions of different engineering tools with external third-party codes for the optimisation process have been eliminated.

The optimisation simulation in WB is straightforward with the steps described in the following section. For a graphical flow work of the optimization problem steps in WB consult Figs. 6 and 8.

Step 1: Geometry design parameters are introduced in Excel, Design Modeller (DM) or other ANSYS modules, and are automatically brought into WB.

Step2: Those design parameters are then linked to optimisation goal parameters that can be defined in any corresponding modules of ANSYS (Excel, FLUENT, etc.), depending on the goal definitions and approaches for their calculations.

Step 3: The relationship between independent parameters (definition of dependent parameters) as well as definition of any new independent parameters and goals which could not have been defined in the previous steps, are accomplished in the "Parameter Set" block. Then, the defined modules for design parameters and goal calculations are linked to the DX module, which is a response surface-based optimisation tool.

Step 4: The lower and upper limits of each parameter are set in "Design of Experiments". Then, an adequate number of design points are generated based on the combination of defined parameters. Finally, each individual design point is evaluated in a numerical investigation to determine its corresponding optimisation goal parameters (objectives).

Step 5: Mathematical response surfaces are fitted through the objective results of previous step.

Step 6: A predefined numerical algorithm looks for optimum region(s) on the generated response surfaces.

The next sections describe the tools and modelling that were applied to calculate the economic, thermal and optical objectives.

2.3. *Economic modelling*

Various independent factors and goals, such as plant efficiencies, resource consumption, environmental impacts and CO_2 emissions, can affect the economic optimisation of energy technologies. However, considering most of these factors and trying to internalise their costs and negative effects on the environment requires appropriate weighting factors, as well as evaluation criteria that are mostly difficult to quantify. Moreover, these factors are usually influenced by the political conditions of local communities and cannot easily be determined on a global level due to their influence on investment decisions. If an actual cost penalty of an environmental impact (e.g., for a clean-up of the technology at the end of the plant's life cycle) or a specific cost benefit (e.g., a tariff rebate because of a CO_2 emission savings) can be quantified, they can be included in the present analysis and tool set. The current work focuses on a purely monetary and financial evaluation of the technology assuming that these case-specific data are not available. The strategy to tackle the economic investigation of this study is according to the economic approach followed by Mertins in his PhD study (Mertins, 2009) with a slight modification.

Therefore, the focus of the economic study is minimising the electricity production costs of an LFC plant. Indeed, the electricity production costs, quantified here as LEC, is a technical term used to calculate the average annual cost per kilowatt hour of electricity. In other words, LEC is calculated as the ratio of the total annual cost over the annual electrical yield of a plant. This term is affected by the different design parameters of a plant, which are clarified in the following sections. A more detailed discussion of the assumption and theory of this study can be found in Mertins (2009).

2.3.1. *Cost assumptions*

Before discussing cost assumptions, it is worth discussing the difference between price and cost. Cost usually quantifies financial expenses, while price is the value that is determined by supply and demand in the market. Therefore, as was mentioned before, this study focuses on the expenses of plants. Moreover, the real costs of an LFC project can ultimately be determined when a commercial LFC project has been completed and its performance published in open access sources. As reported on the website of the National Renewable Energy Laboratory (NREL) (NREL, 2016), the number of LFC projects around the world are limited (12 projects) and these projects are mostly under development. There is limited information about the detailed costs of a plant in demonstration/pilot and commercial projects. Therefore, to make a realistic cost assumption, it seemed appropriate to take the detailed costs of the Solarmundo project (Bernhard et al. (2008)) and to rationally modify those costs to estimate the cost of the design parameters in this study. The following categories were considered to describe the major direct costs of an LFC plant.

- Mirror cost (C_m)

The factors that play a role in the specific cost of a mirror per unit length for a plant could be the mirror itself, its mounting and elevation, storage and transportation, the driving motors (stepper motors) and controllers, and its assembly. This cost is defined as C_m and reported per unit width of mirror. The mirror cost in the Solarmundo project (C_{m0}) was 30.5 €/m for half a metre of mirror width (Mertins, 2009).In this study, mirror curvature has a minor effect due to the high focal length, therefore, reflective material area is mainly dependent on mirror width. So, in this study, mirror cost (C_m) scaling was assumed to be a linear coefficient of (C_{m0}) as defined in Eq. (3). The mirror width, W, is indicated in Fig. 4a.

$$C_m = C_{m0} * \left(\frac{W}{0.5[m]} \right) \tag{3}$$

- Mirror distance cost (C_d)

In order to reduce the shading and blocking effects, adjacent mirrors are installed on a common structure with a gap distance G (see Fig. 4a) defined as the mirror pitch (P) minus the mirror width (W), i.e., the gap when the mirrors are all facing vertically upwards. The specific mirror distance cost per unit length is reported as C_d in this study. This cost in the Solarmundo project (C_{d0}) was 11.5 €/m^2 for a 0.01 m mirror distance (Mertins, 2009). It is evident that by changing this gap, the material cost of the structure, as well as land occupation, is varied. Therefore, it would be rational to assume that C_d is scaled linearly using C_{d0} as in Eq. (4).

$$C_d = C_{d0} * \left(\frac{G}{0.01[m]} \right) \tag{4}$$

- Elevation cost (C_e)

The receiver is mounted at a distance H over the mirror field (see Fig. 4a). The specific cost of mounting the receiver at that elevation is C_e. This cost is reported per unit length and unit elevation. The elevation cost adaptation was exponentially related to the correspondence cost in the Solarmundo projects (C_{e0}=19.8 €/m^2) as introduced by Mertins (2009), according to Eq. (5).

$$C_e = C_{e0} \left(\frac{OD}{0.219[m]} \right)^{n_{ce}} \tag{5}$$

where the exponent n_{Ce} is calculated via Eq. (6). The Mertins formulation (Mertins, 2009) is adapted by modifying the exponent n_{Cr} (Eq. (6)) by the inclusion of an N_t factor, which denotes the number of tubes. Mertins considered a mono-tube. The use of the tube diameter as cost factor is motivated by the fact that the tube diameter is directly linked to the tube wall thickness and therefore the total weight and crane lifting capacity is related to the tube diameter and number of tubes.

$$n_{Ce} = \frac{\ln\left\{\sum \frac{C_i \times N_t}{C_{e0}} \left(\frac{OD}{0.219[m]}\right)^{n_{ci}}\right\}}{\ln\left(\frac{OD}{0.219[m]}\right)} \tag{6}$$

Table 1 contains the values used in Eq. (6).

Table 1
Elements of elevation cost in Eq. (6).

	n_{Ci}	C_i [€/m]
Construction	1.4	14.2
Transportation and packing	1	0.9
Assembly	1	4.6

- Receiver cost (C_r)

The main factors that play a role in receiver costs are the absorber tube, coatings, welding and construction, assembly and transportation. The specific cost of the receiver per unit length is defined as C_r in this study (see Eq. (7)). This cost in the Solarmundo project (C_{r0}) was 654 €/m for a mono-tube receiver with tube outer diameter 0.219 m .The N_t factor, which denotes the number of tubes, is again included in Eq. (8).

$$C_r = C_{r0}\left(\frac{OD}{0.219[m]}\right)^{n_{cr}} \tag{7}$$

$$n_{Cr} = \frac{\ln\left\{\sum \frac{C_i \times N_t}{C_{r0}} \left(\frac{OD}{0.219[m]}\right)^{n_{ci}}\right\}}{\ln\left(\frac{OD}{0.219[m]}\right)} \tag{8}$$

Table 2 contains the values used in Eq. (8).

Table 2
Elements of receiver cost.

	n_{Ci}	C_i [€/m]
Absorber tube	2	116.2
Selective coating	0.9	56.6
Welding	0.7	116.4
Construction	1.4	136.5
Transportation and packing	0.6	26.4

Assembly	0.6	112.6

Combining the above, the direct specific cost of a collector [€/m^2] is:

$$C_c^d = \frac{C_m \times N_m + C_e\,(4 + H\,) + C_d\,(\,N_m - 1\,)G + C_r}{N_m \times W} \tag{9}$$

where N_m denotes the number of mirrors and the cost of the land and its preparation are excluded from the direct cost as it is included later under indirect costs. The reason for considering $C_e(4+H)$ in the collector-specific cost formula is that the mirror fields are mounted 4 m above the ground (Mertins, 2009). The receiver is therefore effectively mounted at $(H+4)$.

In addition to the direct costs of an LFC, the indirect costs of the plant could be outlined as the piping, infrastructure, land cost, project effort, uncertainties, power plant unit, operating and maintenance, and insurance.

By considering a fixed power plant unit, almost all the above parameters would be fixed and independent from the properties of the collector, except land cost. The suggested land cost function is (Mertins, 2009):

$$land\ Cost = C_l \times N_m \times W \times \left(1 + \frac{G}{W}\right) \tag{10}$$

where C_l is the land cost factor.

Therefore, the indirect costs used are reported in Table 3.

Table 3
Indirect costs of a 50 MW linear Fresnel power plant (Mertins (2009))

Name	Cost	Unit	Other
Land costs (C_l)	3	[€/m^2]	Including land acquisition and preparation
Piping (γ_P)	4 002	k€	Plant total cost, including piping, stem traps, etc. "k" refers to "thousands"
Power plant unit (γ_{PU})	33 600	k€	Plant total cost, considering the turbine, feed water tank, a one-stage pre-heater, condenser, generator, etc.
Infrastructure (γ_I)	640	k€	Including building for staff and spare parts, as well as site development
Annuity factors (κ_a)	9.368%		This is a percentage of the total investment and was considered for a duration of 25 years with an interest rate of 8%
Project efforts (κ_e)	22.5%		This is a percentage of the total investment and includes engineering effort, project management, contractor and licensor rights
Operation and maintenance $(\kappa_{O\&M})$	2%		Percentage of total investment
Insurance (κ_i)	1%		Percentage of total investment
Uncertainties (κ_u)	5%		Percentage of total investment

Therefore, the total investment of an LFC plant is:

$$\gamma_{Total\ investment} = \left[C_c^d \times N_m \times W \times (1+\kappa_e) + C_l \times N_m \times W \times \left(1+\frac{G}{W}\right) + \gamma_I \right] \times (1+\kappa_u) + \gamma_{PU} \qquad (11)$$

Therefore, by the annual distribution of total investment cost and considering insurance premiums, personnel and spare parts costs, the total annual cost of the plant is:

$$\gamma_a = (\kappa_a + \kappa_i + \kappa_{O\&M}) \times \gamma_{Total\ investment} \qquad (12)$$

The LEC is defined as the total annual cost of the plant over the annual electrical yield of the plant

$$LEC = \frac{\gamma_a}{\int\limits_{throughout\,a\,year} E_{el}\, dt} \qquad (13)$$

Assuming a fixed electricity output of the plant (constant power plant unit and infrastructure) on the one hand, and the existence of constant terms and coefficients in Eqs. (11) to (13**)** on the other hand, one can consider that the terms that play a role in the minimisation of the LEC are:

$$\gamma_{Plant\,Cost\,Factor} = C_c^d \times N_m \times W \times (1+\kappa_e) + C_l \times N_m \times W \times \left(1+\frac{G}{W}\right) \qquad (14)$$

where $\gamma_{Plant\,Cost\,Factor}$ comes from the first two terms on the right hand side of Eq. (11).

The authors would not claim this to be the best goal definition for the economic optimisation of Fresnel collectors, but at least it would give future researchers a first rough optimisation goal for finding a utopian region in this process. In addition, defining a realistic LEC goal as the optimisation goal would be a complex issue especially when this goal must meet industry needs. Such a realistic optimisation goal definition would require a lot of information on the economic aspects of linear Fresnel projects that, due to a lack of data on Fresnel plants in open access sources, would be almost impossible.

Therefore, in future economic optimisation studies that need more accurate and complex economic objectives (i.e. industrial projects), it is recommended that researchers stick to the discussed goal as a first estimation in their economic optimisation investigations and then try to define and apply other complex economic goals as the next step in their optimisation process.

2.4. Thermal modelling

Two approaches were considered in the optimisation of heat loss from the cavity receiver. These approaches were view area simulation and CFD simulation. The first was defined as a goal to speed up the expensive process of the whole collector domain optimisation, while the second was chosen for the insulation optimisation of the cavity receiver.

The fact should be considered that calculating heat loss via a view area is not as accurate as a CFD simulation. To justify this assumption, consider the response surface method (RSM) – the optimisation process followed in this study. In order to capture an accurate response surface, the optimisation process needs an adequate number of design points, which are generated via numerical algorithms. Then, for each individual design point, the goals have to be modelled and calculated via their corresponding tools. Now assume that for the collector optimisation process, heat loss is calculated via CFD tools. As will be explained later, for collector domain optimisation, more than 1 800 design points are needed. Assuming one hour as the computational time needed for each CFD simulation, the calculation of heat loss goal alone would take about two and half months, without considering the computational cost to calculate other goals and the optimisation process. Therefore, introducing a simplified approach to tackle the heat loss calculation with acceptable accuracy is justified.

The view area approach and the more accurate CFD approach are now discussed.

2.4.1. View area approach

The justification for this approach is the assumption that radiation is the most dominant heat loss mechanism. This was proved both experimentally (Jance et al., 2000; Reynolds et al., 2004; Flores Larsen et al., 2012) and numerically by previous researchers (Moghimi et al., 2014; Moghimi et al., 2015c; Facão and Oliveira, 2011). Dey (2004) claimed that the radiative loss constitutes about 80% of the total heat loss from the absorber. Hence, it is rational to optimise heat loss by minimising radiative heat loss. Moghimi et al. (2015c) showed that most of the cavity heat loss dissipates from the bottom glass as a result of re-radiation from the absorber tubes to the mirror field. Therefore, as a simplifying assumption, one can assume that minimising the absorber tube areas that face the mirror field (view area of absorber tubes to mirror field) would minimise thermal loss. View area is directly proportional to view factor, which is a well-known radiative term in heat transfer textbooks. According to Cengel and Ghajar (2010), the view factor is the fraction of radiation leaving surface i that strikes surface j directly.

The following relationships between parameters have to be defined for the defining view area. Refer to Fig. 4-b by considering an N_t-tube's tube bundle with tube pitch *m,* which is located centrally in the cavity. Then:

$$2p + (N_t - 1) \times m = 0.332 \tag{15}$$

where N_t is the number of tubes in the cavity. Therefore,

$$p = 0.5 * \left[0.332 - (N_t - 1) \times m\right] \tag{16}$$

where p is the horizontal distance of the first/last tube from the closest cavity's bottom corner. Then the horizontal distance of the i_{th} tube centre from the cavity's left bottom corner ($q_{i_{th}\ tube}^{left}$) is:

$$q_{i_{th}\ tube}^{left} = p + (i-1) * m \tag{17}$$

where i is the tube counter from the left side. Therefore, the distance of the i_{th} tube centre from the cavity's right bottom corner is:

$$q_{i_{th}\ tube}^{right} = 0.332 - q_{i_{th}\ tube}^{left} \tag{18}$$

In addition, the angle of the tangential line with the tube bundle line is named β. The tangential line is defined as a line that passes through the i_{th} tube centre and coincides with the circumference of the adjacent tube. Since β is a fixed property (due to the fixed tube radius and pitch), its specification is independent of the tube counter.

$$\beta = \sin^{-1}\left(\frac{r}{m}\right) \tag{19}$$

For defining the area of a tube that faces the mirror field, one has to consider the constraint factors that confine view area: proximity of the adjacent tube and the tube centre distance from the left and right corners. Therefore, two central angles for each individual tube were defined ($\alpha_{i_{th}\ tube}^{left}$ and $\alpha_{i_{th}\ tube}^{right}$) to capture the view area. These central angles for the i_{th} tube are:

$$\alpha_{i_{th}\ tube}^{left} = Min\left[\left(\frac{\pi}{2} - \beta\right), \tan^{-1}\left(\frac{q_{i_{th}\ tube}^{left}}{h-d}\right)\right] \text{, except for the left-most tube, which has}$$

$$\alpha_{1_{st}\ tube}^{left} = \tan^{-1}\left(\frac{q_{1_{st}\ tube}^{left}}{h-d}\right) \text{ where } q_{1_{st}\ tube}^{left} \text{ equals } p \text{ (Eq. (16))} \tag{20}$$

$$\alpha_{i_{th}\ tube}^{right} = Min\left[\left(\frac{\pi}{2} - \beta\right), \tan^{-1}\left(\frac{q_{i_{th}\ tube}^{right}}{h-d}\right)\right] \text{, except for the right-most tube, which has}$$

$$\alpha_{N_{t\,th}\ tube}^{right} = \tan^{-1}\left(\frac{q_{N_{t\,th}\ tube}^{right}}{h-d}\right) \text{ where } q_{N_{t\,th}\ tube}^{right} \text{ equals } p \text{ (Eq. (16))} \tag{21}$$

In Fig. 4-b, the confining angles for the left side of the i_{th} tube are shown in blue and red. These help explain why the minimum function was used in Eqs. (20) and (21) to define $\alpha_{i_{th}\ tube}^{left}$ and $\alpha_{i_{th}\ tube}^{right}$.

So, the view area of the i_{th} tube per unit length is:

$$viewarea_{\ i_{th}\ tube} = r \times \left(\alpha_{i_{th}\ tube}^{left} + \alpha_{i_{th}\ tube}^{right}\right) \tag{22}$$

with *r* being the tube radius.

Therefore, minimisation of tube bundle radiation loss is possible by minimising the total view area of the tube bundle per unit length:

$$viewarea\,of\ tubebundle = \sum_{i=1}^{N_t} viewarea_{\ i_{th}\ tube} \tag{23}$$

2.4.2. CFD approach

The CFD simulation approach that is applied for the insulation optimisation of this study is a duplication of the approach introduced by Moghimi et al. (2014; 2015c) to conduct the heat loss calculation. In this CFD investigation, a two-dimensional (2D) snapshot of the cavity is simulated. This 2D modelling simulates the steady-state cross-section of the cavity receiver at a certain tube temperature. Moghimi et al. (2015c) proved that the thermal simulation of a multi-tube trapezoidal cavity receiver can be performed with a constant circumferential temperature assumption as the driving thermal source in the cavity. To prove this, Moghimi et al. (2015c) simulated a 3D cavity with a non-uniform solar heat load on the tubes as obtained from a SolTrace ray-tracing simulation. Heat loss comparison of these two cases proved that a 2D simulation with a constant temperature assumption can accurately model the heat loss from a cavity (for a detailed discussion of the comparison and its findings please consult Moghimi et al. 2015c; 2015d). This assumption has been widely used by previous researchers without checking its validity (Haberle et al., 2002; Pye, 2008; Facão and Oliveira, 2011; Sahoo et al., 2012; 2013a; 2013b; Lai et al., 2013; Manikumar et al., 2014; Heimsath et al., 2014).

Moreover, previous researchers mostly used the Boussinesq approximation to simulate natural convective flow inside the cavity enclosure (Pye, 2008; Facão and Oliveira, 2011; Sahoo et al., 2012; 2013a; 2013b; Lai et al., 2013) without verifying this assumption. According to ANSYS (2013), this approximation is accurate when the actual change in density is small $\left(\frac{\Delta\rho}{\rho} << 1\right)$. Natrajan et al. (2012) and Manikumar et al. (2014) explicitly mentioned that in linear Fresnel cavity cases, where surfaces can reach temperatures of more than 100 °C, the Boussinesq approximation will not give accurate numerical results. Therefore, Moghimi et al. (2015c) suggested the incompressible ideal gas assumption for fluid density variation inside the cavity. The researchers checked the validity of that model and proved that the incompressible ideal gas assumption is valid for cavity receivers.

In terms of radiation heat transfer simulation in the cavity, Natrajan et al. (2012) and Manikumar et al. (2014) used the surface-to-surface (S2S) model, which applies view factors and is applicable for the simplified simulation of a domain. Moghimi et al. (2014; 2015a; 2015b; 2015c; 2015d) suggested the more accurate discrete ordinates method (DOM). The DOM is computationally more expensive than the S2S model, but is more accurate and can predicate complex heat transfer phenomena inside the cavity domain. These researchers showed that, with the help of this method and defining two non-gray bands in a domain, two complex physical interactions of radiation in the domain can be captured: specular and diffuse reflections from surfaces due to surface roughness, and the wavelength-dependent opaqueness of glass, which leads to the greenhouse effect inside the cavity.

In this study, the CFD settings, material properties and boundary conditions were set according to the method discussed in Moghimi et al. (2015c). A summary of that information is reported in Table 4 and Table 5. The tube bundle temperature of 500K is on the same order as the outlet temperatures of commercial and demonstration LFC plants (Moghimi (2016)). As a comparison, Flores Larsen et al. (2012), Manikumar et al. (2014) and Singh et al. (2010) considered maximum temperatures of 558K, 450K and 523K, respectively, in their LFC studies. The effect of the current temperature choice is investigated to some extent below when the heat losses throughout the plant (where the temperature is steadily rising) are quantified.

Table 4
Material properties.

Material	**Density [kg/m^3]**	**Specific heat [J/kg-K]**	**Thermal conductivity [W/m-K]**	**Other**
Air in cavity (Lienhard IV and Lienhard V, 2003)	Incompressible ideal gas	Piecewise linear function of temperature	Piecewise linear function of temperature	Viscosity [Pa.s]: Piecewise linear function of temperature
Semi-transparent glass	2 650	786	1.5	Refractive index = 1.5, absorption coefficient [m^{-1}] ϵ (106; 2 300) for wavelength (below 4.25μm; above 4.25μm)
Insulation-glass wool (TIASA, 2001)	48	446	Piecewise linear function of temperature	-

Table 5
Boundary condition values

Surface	**Velocity components [m/s]**	**Temperature [K]**	**Heat transfer coefficient [W/m^2-K]**	**Emissivity**
Tube bundle outer surface	0, 0	500	-	0.95 in lower wavelength band and 0.1 in higher wavelength band
Top, side walls	0, 0	-	-	0.05
Glass inner side	0, 0	-	-	0.9
Glass outer side	-	300 (convection, ambient Temp.), 305 (radiation, surrounding Temp.)	5	0.75
Insulation outer side	-	300 (convection, ambient Temp.), T_{sky}=0.0522* $300^{1.5}$ (radiation, sky Temp.)	5	0.75

2.5. Optical modelling

One of the optimisation goals that are considered in this study is daily solar power, which is defined as the average solar power received by all tubes of the receiver throughout a summer day. For the daily calculation of incident solar power for a defined case, this study considers 11 optical simulations on an LFC throughout a summer day. In other words, the optical simulation results for every 15 degrees of sun position in a transversal plane (ζ in Fig. 4-a), are used. Therefore, the net incident power on each tube for the specified sun directions is calculated and exported to an Excel file. Then, the summation of all those incident powers on tubes is the total incident solar power the cavity receiver absorbs at a single sun position. Finally, by calculating the total incident solar power for other sun positions along a day and obtaining the average, the daily solar power is calculated. After setting the optimisation goal, the appropriate engineering tools for calculating net power output on absorbers have to be surveyed.

Moghimi et al. (2015a; 2015b; 2015d) proved that CFD simulation for different cases of optical modelling of solar domains is as accurate as ray-tracing (an approach widely used by researchers) and tried to show the advantages of a CFD approach for optical simulation. However, based on the required computational time and the high number of design points in the RSM optimisation process, using ray-tracing software is a more rational option for collector optimisation.

Therefore, in this study, SolTrace (a free ray-tracing tool developed by NREL in 2014) was used for optical simulation. The main drawback of this software in comparison with CAD packages is its limited ability in the graphic user interface to introduce multiple and complex elements (for detailed comparison of SolTrace vs. commercial CAD and CFD packages, consult Craig et al. 2016). To address this, Moghimi et al. (2015d) came up with mathematical formulations implemented in Excel for correctly defining elements of the mirror field and their aiming points automatically. This make accomplishment of automation process much easier and prevent laborious manual efforts to precisely calculate the aiming points of each single elements of array of mirrors in an LFC plant, corresponding to a single sun angle. The same process can be performed using scripting in SolTrace, but for the current implementation where the optimisation process is driven from ANSYS Workbench, using Excel which is included as a standard solver in WB as discussed elsewhere, makes more sense. For example, in this study, 11 individual sun positions in the transversal plane (ζ in Fig. 4-a) have to be set for each definite LFC case. This means that 11 separate optical simulations have to be considered throughout a summer day. Therefore, the individual mirror angle in each of those simulations has to be defined according to its spatial location from cavity receiver and sun position. The receiver and the mirror elements were defined in the same SolTrace stage to enable shadowing of the receiver to occur automatically.

Moreover, to get assurance on SolTrace solution convergence, Moghimi et al. (2015d) performed a thorough investigation on the effects of the "desired number of ray intersection" parameter on the stabilisation of heat flux value, as well as its effects on the circumferential distribution of ray hits for each tube. They found that at least one million rays are required for a converged solution for a multi-tube trapezoidal cavity receiver.

Therefore, in this study, the SolTrace settings for optical modelling are defined as used by Moghimi et al. (2015d). Those settings are reported in Table 6. Note that ideal optical properties are mostly used as illustrative of the methodology. A sample SolTrace screenshot is depicted in Fig. 5 as illustrative of the reflective (mirrors and cavity walls) and absorptive (receiver tubes) elements used.

Table 6
SolTrace parameters for LFC optical modelling

Sun shape	Gaussian	2.73 mrad standard deviation	x- and z-direction (components were defined according to sun position angle)
Primary mirrors	Reflectivity = 1	Slope error = 0.0001	Specularity error = 0.0001
Tubes	Reflectivity = 0.05		
Glass	Transmissivity = 1	Refraction ratio = 1.5	
Cavity side walls	Reflectivity = 0.95		
Direct Normal Irradiation (DNI)	1 000 W/m^2		

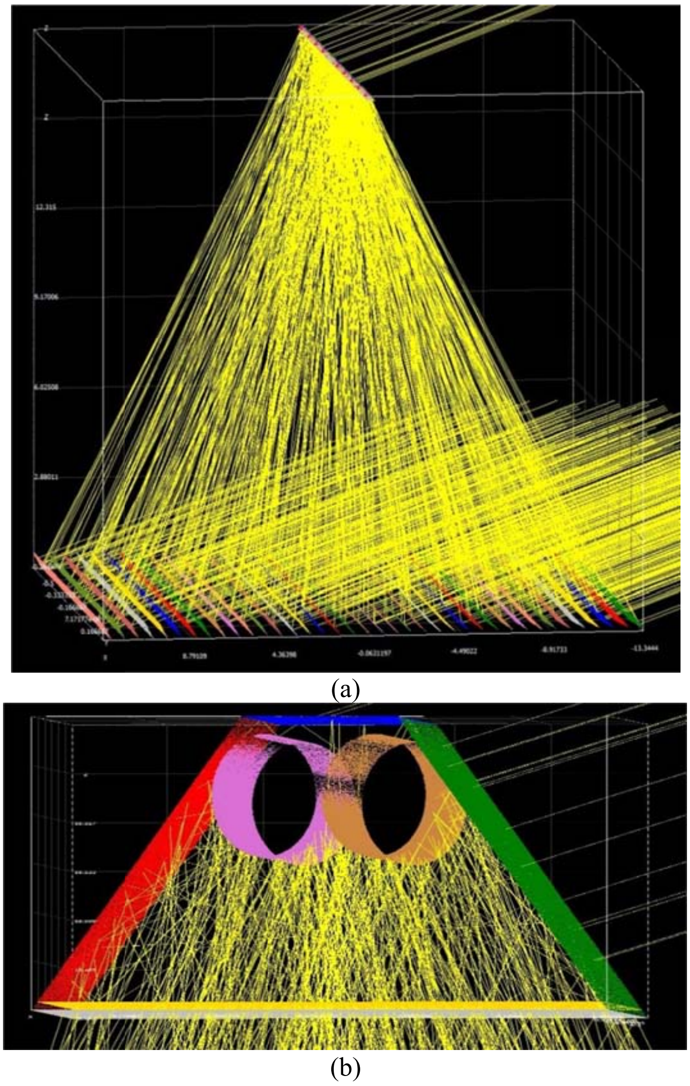

(a)

(b)

Fig. 5. Sample SolTrace rays for a sun angle of 165° for
1 000 000 ray intersections.

(a) Global view. (b) close-up of receiver.

3. Optimisation

3.1. Optimisation problem definition

In this study, an LFC domain is optimised to design a collector that is thermally, optically and economically optimal. Due to the complexity of the optimisation process and the cost of the computational process, a two-stage optimisation process is suggested. In the first stage, the collector domain parameters, except for the insulation thickness parameters, are optimised by considering economic, thermal and optical goals in ANSYS WB. In the second stage, the optimised cavity from the first stage is taken and optimised for its insulation through the minimisation of heat loss and insulation material.

3.1.1. First-stage optimisation problem (collector optimisation)

The set of design variable parameters investigated in this stage of optimisation includes (the notation was defined in Fig. 4): number of mirrors (N_m), mirror width (W), mirror gaps (G), mounting height of cavity or cavity top wall distance from mirror line (H), tube outer radius (r), tube gap (g), tube bundle offset from cavity top wall (d), cavity angle (θ) and cavity depth (h). This set of variables combined tries to find a utopian collector where the total plant cost factor ($\gamma_{Plant\,Cost\,Factor}$) and view area are minimised, while maximising daily solar power.

The definition and calculation of design variable parameters and goals are subsequently described.

The variable set was defined in an Excel file. This variable set was then used in calculations of the total plant cost factor and view area based on formulations in previous sections (sections 2.3 and 2.4.1). However, the calculation of daily solar power is complicated. This calculation is done through an exchange of information between Excel and SolTrace, using coding in Visual Basic for Application (VBA) and the LK scripting language, respectively. These scripting languages are very useful in setting up parametric runs and optimisations. For example the definition of daily solar power was set with the help of these tools in this optimisation study (Please see Fig. 6).

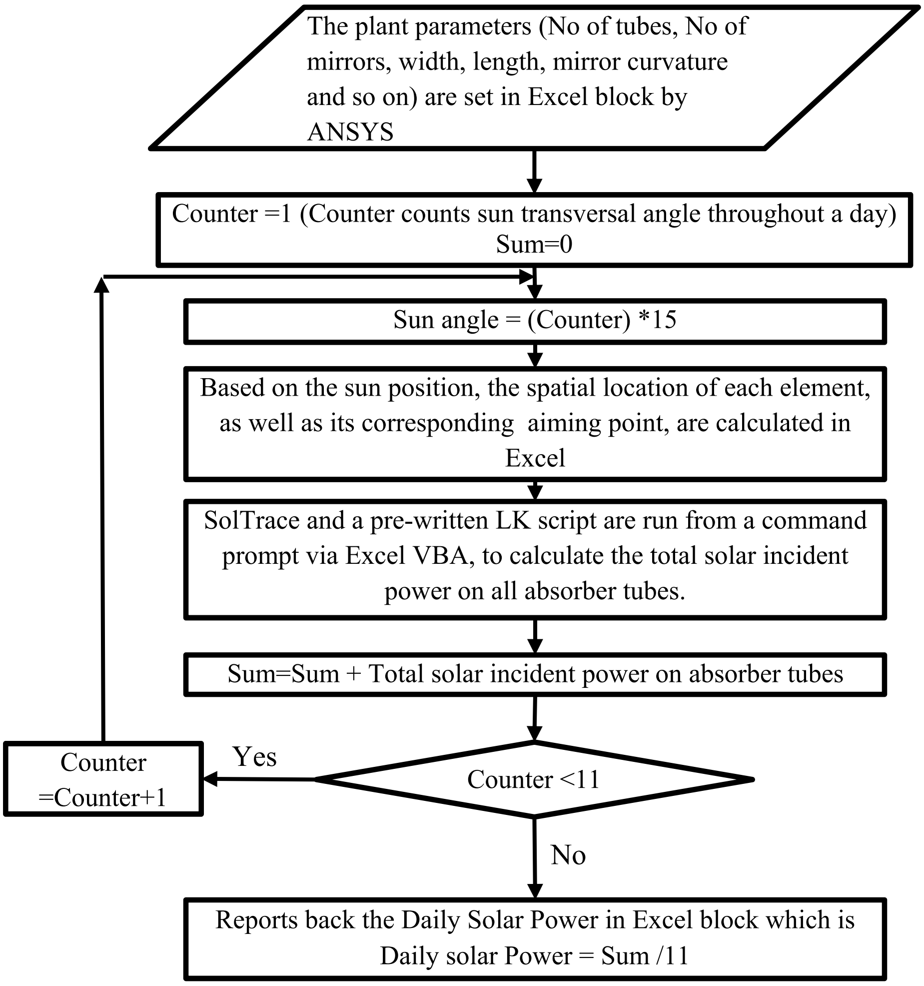

Fig. 6: The flowchart of Daily Solar Power definition.

After defining all design parameter variables and optimisation goals in Excel, the Excel file is linked to DX in WB and the optimisation loop is closed and ready for execution. Fig. 7 shows the optimisation loop in WB.

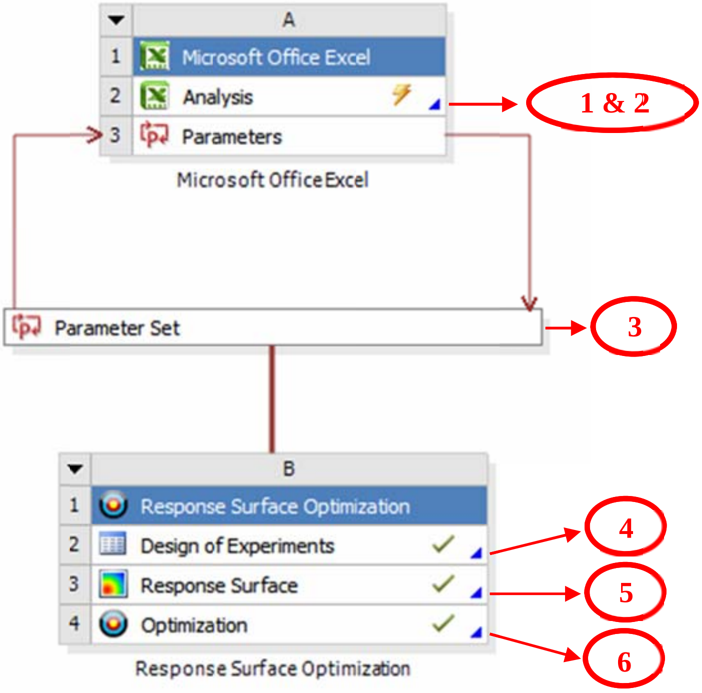

Fig. 7. Optimisation loop for collector optimisation problem in ANSYS WB with inserted step number of optimisation flowchart in the platform.

The optimisation problem of this section is formulated as:

$$\begin{aligned} &Minimize\left(w_1\,ViewArea(\tilde{x}) + w_2\,\gamma_{Plant\,Cost\,Factor}(\tilde{x})\right), \\ &Maximize\left(w_3\ Total\ Daily\ Solar\ Power(\tilde{x})\right) \end{aligned} \tag{24}$$

subject to bounds $\tilde{x}$, where $\tilde{x}$ is the set of design variable parameters.

The weighting factors w_k are implicitly defined based on the Multi-Objective Genetic Algorithm (MOGA) and the optimisation process explained in detail in section 3.2.

The design variable set, allowable ranges and derived parameters are introduced in Table 7.

Table 7
Definition of objective and parameter ranges (notations used in table are based on their definition in Fig. 4)

Independent parameters	**Lower bound**	**Upper bound**	**Other**
Number of mirrors – N_m	10	50	Discrete value and the variation step is 2.
Mirror width – W [mm]	100	1 000	Continuous variation
Mirror gap – G [mm]	10	1 000	Continuous variation
Mounting height of cavity – H [m]	5	20	Continuous variation
Tube outer radius – r [mm]	10	30	Continuous variation
Tube gap – g [mm]	1	4	Continuous variation
Tube bundle offset from cavity top wall – d [mm]	25	50	Continuous variation
Cavity angle – θ [degree]	50	90	Continuous variation
Cavity depth – h [mm]	100	150	Continuous variation
Dependent parameters	**Relation**		
Tube outer diameter – OD	$OD = 2 \times r$		
Tube pitch – m [mm]	$m = OD + Tube\ Gap$		

Number of tube absorber $-N_t$	$N_t = Round\, down\left\{ \frac{1}{m} \times \left[332 - 2\left(\frac{h-d}{tan\theta} \right) \right] \right\}$	Derived parameter with integer output constraint
Focal length of j_{th} mirror	$f_j = \sqrt{X_j^2 + Z^2}$	Where X_j is the distance of the j_{th} mirror centre to the collector symmetry line and Z is the perpendicular tube bundle distance from the mirror field. Therefore, for an N_m mirror field, $N_m/2$ focal lengths have to be determined.
aperture [mm]	332	Fixed constraint

Optimisation objective	**Relation**	**Objective**
Heat loss	View area of tube bundle	Minimisation
Plant cost	$\gamma_{Plant\, Cost\, Factor}$	Minimisation
Solar power	Daily solar power	Maximisation

3.1.2. Second-stage optimisation (insulation optimisation)

This optimisation stage was defined to optimally insulate the cavity of the previous stages in the optimum collector. The set of design variables of this optimisation study (refer to Fig. 8) are side insulation thickness (*b*), top insulation thickness (*t*), and top insulation angle (δ). In this optimisation study, minimising the cavity heat loss and minimising the insulation area were considered as the thermal and economic goals of optimisation.

Since the cavity properties (i.e. number of tubes, tube diameter, tube locations, etc.) were determined in section 3.1.1 and are fixed in this study, the view area approach defined in the section 2.4.1 is not applicable. In this study, the proposed tool for the calculation of the thermal performance is the CFD approach (section 2.4.2) in WB, while the calculation of the insulation area as an optimisation goal was done by introducing Eq. (30) into DX. In the CFD approach, the radiation heat loss is modelled using the Discrete Ordinates method with radiative properties specified for two wave-length bands. This means that the glass window has a band-selective absorption as defined in Table 4.

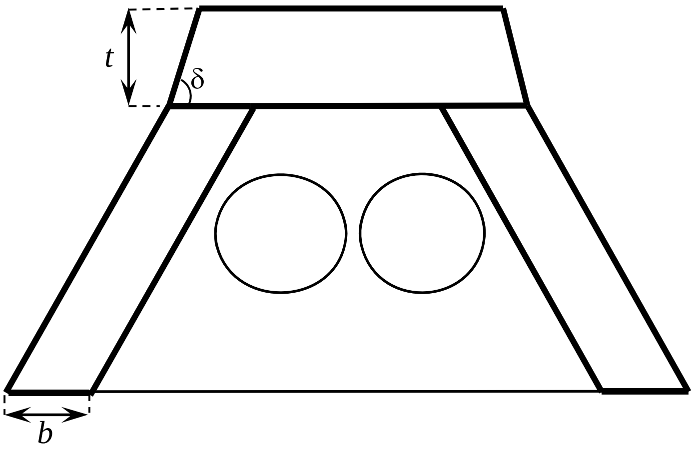

Fig. 8. Variation definition in insulation optimisation. The cavity parameters are those determined in the previous optimisation study.

Fig. 9 shows the optimisation loop of this study in WB. The proposed geometry (Fig. 8), as well as the design variable parameters, was set in the ANSYS CAD module DM. The defined domain was then meshed in the ANSYS meshing tool and then linked to the ANSYS CFD tool, FLUENT, where the net heat loss from the cavity boundaries is calculated and linked to DX for the optimisation study.

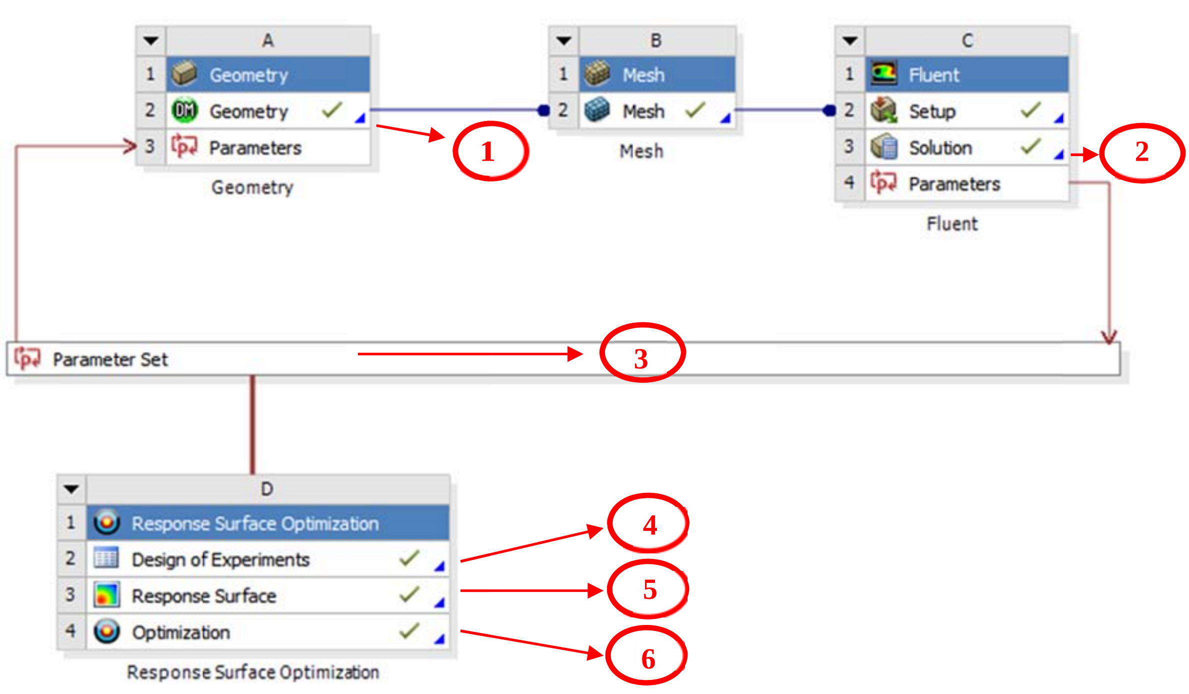

Fig. 9. Optimisation loop for the insulation optimisation problem in ANSYS WB with inserted step number of optimisation flowchart in the platform.

The optimisation problem of this section is:

$$\begin{aligned}&\min imize\left(w_4 f_4\left(\tilde{x}\right)+w_5 f_5\left(\tilde{x}\right)\right)=\min imize\left(w_4 heatloss\left(\tilde{x}\right)+w_5 Insulationarea\left(\tilde{x}\right)\right)\\&Subjecttobounds\tilde{x}\ with\tilde{x}=\left(b,\delta,t\right)\end{aligned} \tag{25}$$

The allowable ranges of the design variables are listed in Table 8.

Table 8
Definition of objective and parameter ranges (notations used in the table are based on their introduction in Fig. 8 and Fig. 4)

Independent parameters	**Lower bound**	**Upper bound**	**Other**
Side insulation thickness – *d* [mm]	25	100	Continuous variation
Top Insulation Thickness- *e* [mm]	10	60	Continuous variation
Top insulation angle – δ [degree]	40 °	90 °	Continuous variation
Dependent parameters	**Relation**		

Tube outer radius – *r*, tube gap – *g*, tube bundle offset from cavity top wall – *d*, cavity angle – θ , cavity depth – *h*, tube outer diameter –OD, tube pitch – *m*, number of tube absorber – N_t, aperture	Fixed constraint		The implemented values in this optimisation study were as per the proposed optimum case results of section 3.1.1.
Optimisation objective	**Relation**	**Objective**	
Heat loss from boundaries	Summation of heat losses from outer boundaries	Minimisation	If the losses are reported as an absolute value, then the goal is the minimisation of losses; however, if the losses are defined as a negative value (the way in which it is reported in ANSYS FLUENT), then the goal should be maximised.
Insulation area	$Total\,area = 2\times h\times b + 2\times b\times t - \frac{t^2}{tan\,\delta} + \left(332 - \frac{2\times h}{tan\,\theta}\right)\times t$ $\left[mm^2\right]$	Minimisation	Where *h* and θ are substituted by 144 and 51 respectively (the results of the optimum cavity in section 4.1). The mathematical formulation was discussed in more detail in supplementary section 6.1.

3.2. *Optimisation algorithm and settings*

The following features of ANSYS DX were used for the optimisation. The RSM was chosen for the mathematical optimisation. The design of experiments (DOE) was performed using Latin hypercube sampling design applied to a specific number of design points. The number of design points is automatically determined according to combinations of the optimisation independent parameters based on the DOE type and sampling algorithm. For each of three optimisation problems, the number of design points and independent parameters are reported in Table 9.

Table 9
Number of design points and independent parameters for different optimisation problems

Optimisation problem	Design points	Independent Variables	DOE type	Sample type
First problem (collector optimisation – Section 3.1.1)	1 881	9	Latin hypercube sampling	Central Composite Design (CCD)
Second problem (insulation optimisation for determined cavity – Section 3.1.2)	15	3	Latin hypercube sampling	CCD

In each of the optimisation problems (sections 3.1.1 and 3.1.2), the corresponding engineering tools and calculations are run to extract the allocated goals of that problem for each individual design point. Then, the construction of response surfaces is performed using a full second-order polynomial for the first optimisation problem and Kriging for the second problem. The determination of the optimum location on these surfaces was done using MOGA. This method results in a Pareto optimal set given competing objectives. This set represents the family of optimal designs of the combined objective response surfaces through the variation of the relative weighting of the competing objectives. The MOGA settings for each of these optimisation problems are tabulated in Table 10.

Table 10
MOGA settings for different optimisation problems.

Optimisation problem	**Number of initial samples**	**Number of samples per iteration**	**Maximum allowable Pareto percentage**	**Maximum number per iteration**
First problem (collector optimisation – Section 3.1.1)	200	200	90%	200
Second problem (insulation optimisation for determined cavity – Section 3.1.2)	50	50	90%	100

A detailed discussion on the salient features of the Kriging, MOGA and optimisation algorithm are presented in Moghimi et al. (2015c).

4. Results and discussion

4.1. *Optimisation results for the first problem (collector optimisation)*

The optimisation on the combined Kriging response surfaces converged after 2 936 iterations, considering a higher importance for the daily solar power objective and a default importance for the other objectives (view area of tube bundle, γ plant cost factor). In addition, a strict constraint (values greater than 0) was set on the plant cost objective to force optimisation convergence to a physically meaningful value.

To show the effect of independent parameters on optimisation objectives, twelve 3D response surfaces are presented in Fig. 10 to Fig. 12. These response surfaces are presented for the introduced independent parameters under the chosen feasible optimum case column in Table 11. Due to the impossibility of physically displaying a surface in more than three dimensions, these 12 surfaces were broken up into three groups of four, which are displayed in three consecutive figures (Fig. 10 to Fig. 12). In those figures, the independent parameters are held constant at their optimum values when not plotted in a particular sub-figure. In Fig. 10, Fig. 11 and Fig. 12, respectively, the γ plant cost factor, daily solar power and view area of tube bundle objectives are considered fixed, and the effect of each two independent parameters on that objective are shown and discussed.

Fig. 10-a displays the effects of cavity depth and angle on γ plant cost factor. It can be seen that the γ plant cost factor increases by increasing the cavity angle, while the opposite trend is shown for the cavity depth. These two independent parameters affect the available space in

the cavity to house the tube bundle. Increasing the cavity angle transforms the trapezoidal shape of the cavity towards a rectangular shape, which leads to an increase in available space, while for a fixed trapezoidal cavity angle, increasing the cavity depth decreases the available space for the tube bundle (due to the determined location of the tube bundle from the cavity top wall). Hence, the depicted effects displayed in Fig. 10-b make sense physically according to the following reasoning: For a constant tube radius case, by reducing the available location for a tube bundle, the number of tubes in the tube bundle decreases. Reducing tube numbers leads to a cheaper cavity collector due to the cost of the tube, welding tube cost, tube coating cost, etc. Fig. 10-b shows the effect of tube radius and tube gap on the γ plant cost factor. According to the previous discussion, by increasing the tube radius and tube gap, one can expect a decrease in cavity cost, since less tubes can fit into a cavity, as shown in Fig. 10-b. Fig. 10-c indicates that, by increasing the gap between mirrors, as well as the cavity mounting height, the plant cost increases mainly because of the increased land use area and higher supporting structure. Although the effect of the cavity mounting height on the γ plant cost factor may not be as obvious as the effect of the mirror gap in Fig. 10-c, it is proved by observing the colour gradient along a fixed mirror gap. These objective dependencies are also justified by mathematical formulations – Eqs. (9) and (14) – of the plant cost factor term $\left(\gamma_{Plant\ Cost\ Factor}\right)$ where mirror gap (G) affects both the land cost term and the direct specific cost of a collector term (C_c^d), whereas the mounting height only influences the latter term. Finally, the effects of mirror numbers and mirror width on the plant cost factor term are depicted in Fig. 10-d. Note that as the number of mirrors is a discrete variable, the response surfaces (in Fig. 10-d and subsequent figures Fig. 11-d and Fig. 12-d) are a set of slices or lines and thus not continuous. The trend of the response surface in Fig. 10-d makes sense since increasing both the mirror width and the number of mirrors increases the land cost and mirror field cost as discussed.

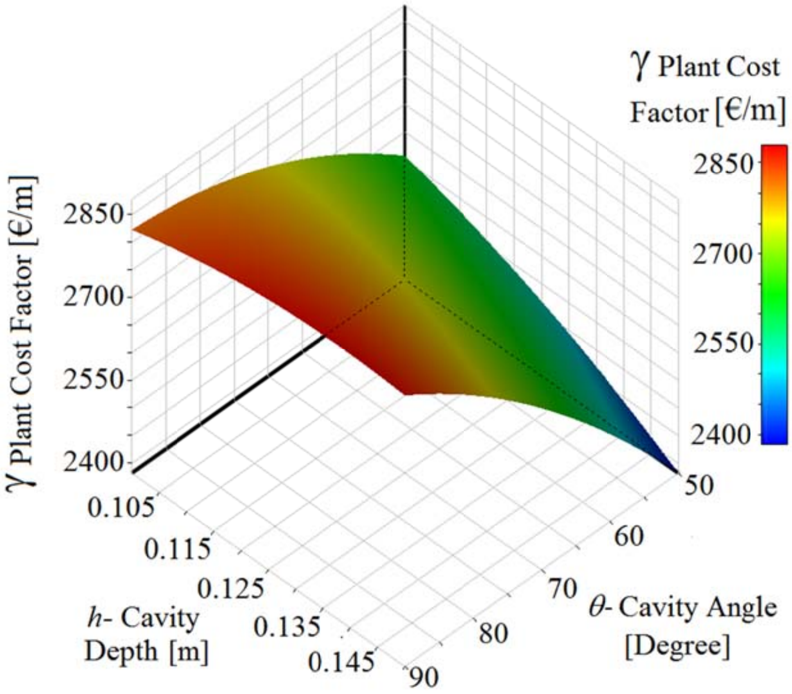

(a)

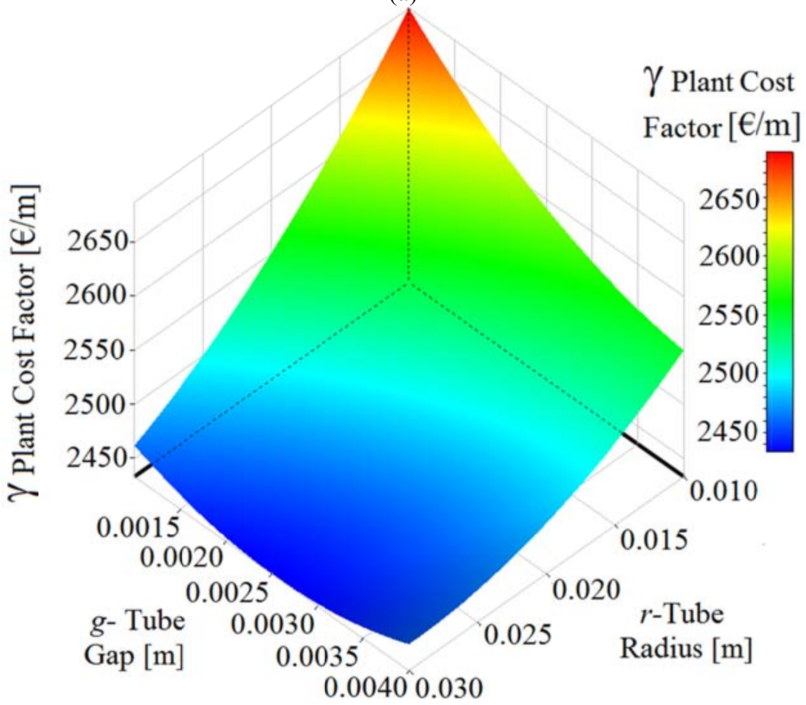
γ Plant Cost Factor [€/m]
2650
2600
2550
2500
2450
γ Plant Cost Factor [€/m]
2650
2600
2550
2500
2450
0.0015
0.0020
0.0025
0.0030
0.0035
0.0040
g- Tube Gap [m]
0.010
0.015
0.020
0.025
0.030
r-Tube Radius [m]

(b)

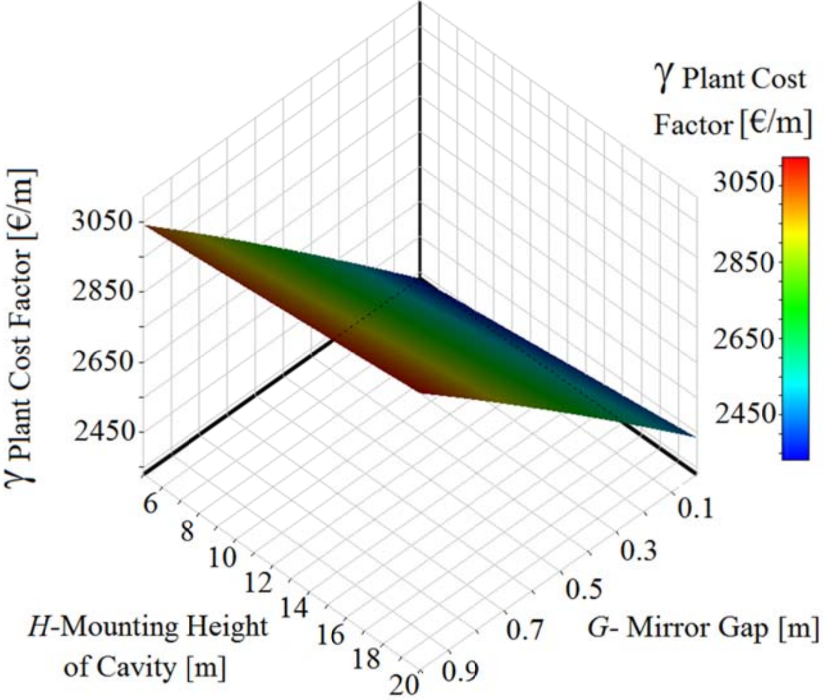
γ Plant Cost Factor [€/m]
3050
2850
2650
2450
γ Plant Cost Factor [€/m]
3050
2850
2650
2450
6
8
10
12
14
16
18
20
H-Mounting Height of Cavity [m]
0.1
0.3
0.5
0.7
0.9
G- Mirror Gap [m]

(c)

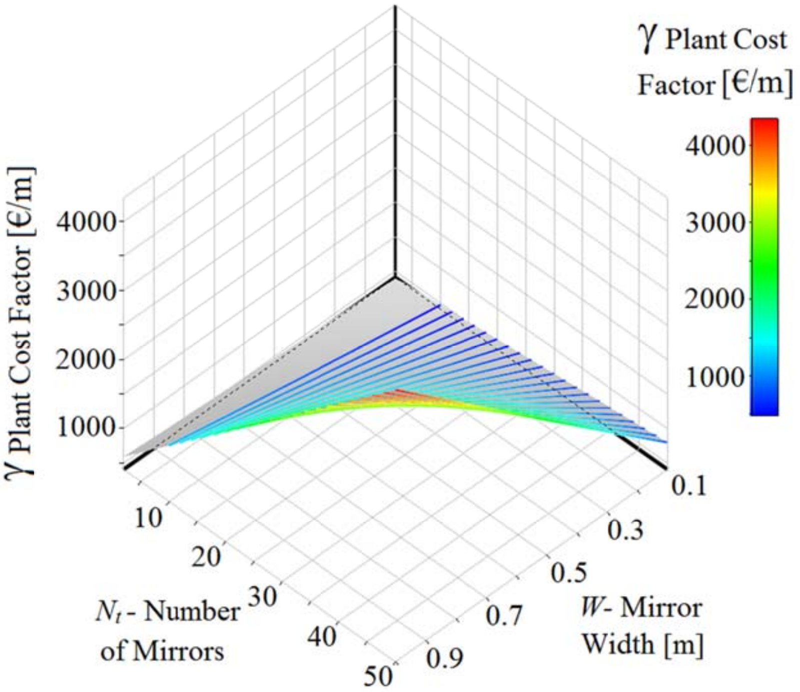

(d)

Fig. 10. Response surfaces of the plant cost factor term vs. independent parameters. a) Plant cost factor vs. cavity depth and cavity angle. b) Plant cost factor vs. tube gap and tube radius. c) Plant cost factor vs. mounting height of cavity and mirror gap. d) Plant cost factor vs. number of mirrors and mirror width.

In the following discussion, the effects of the independent parameters on the objective of the view area of the tube bundle are displayed in Fig. 11-a to 11-d. This objective is reported per unit length of the plant. Fig. 11-a shows the effects of cavity angle and cavity depth on the view area of the tube bundle. Due to the fixed aperture assumption, a decrease in cavity angle or increase in cavity depth would lead to less available space in the cavity for fitting a tube bundle or fewer tubes in the cavity. Therefore, the view area falls. Fig. 11-b depicts the effects of tube radius and tube gap on the view area. As shown in this figure, either increasing the tube radius or the tube gap reduces the view area of the tube bundles, since fewer tubes fit into the cavity. Fig. 11-c and 11-d show the effects of the cavity mounting height, the gap between the mirrors, as well as the number of mirrors and the mirror width on the view area. As expected, the mirror field parameters (i.e. the number of mirrors, the mirror width, the mirror gap and the mounting height of the cavity) have less influence on the view area objective (see range on the vertical axis). Actually, this was an expected fact for those parameters, according to the discussion on view area (section 2.4.1). The physical constraints that limit re-radiation of the tube bundle to the mirror field were the closeness of the tube to the side cavity walls or to adjacent tubes. These constraints are effectively limited by cavity parameters, not by mirror field parameters.

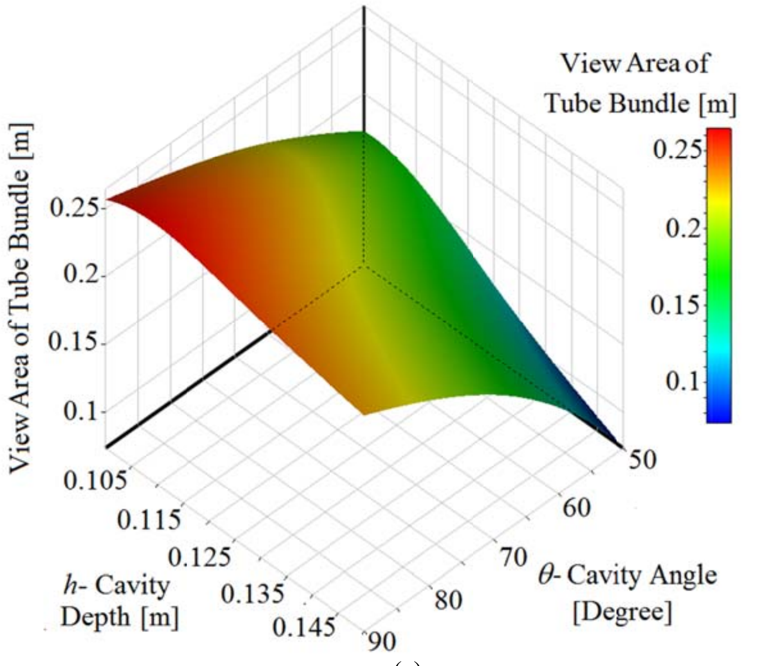
View Area of Tube Bundle [m]
0.25
0.2
0.15
0.1
View Area of Tube Bundle [m]
0.25
0.2
0.15
0.1
0.105
0.115
0.125
0.135
0.145
h- Cavity Depth [m]
90
80
70
60
50
θ- Cavity Angle [Degree]

(a)

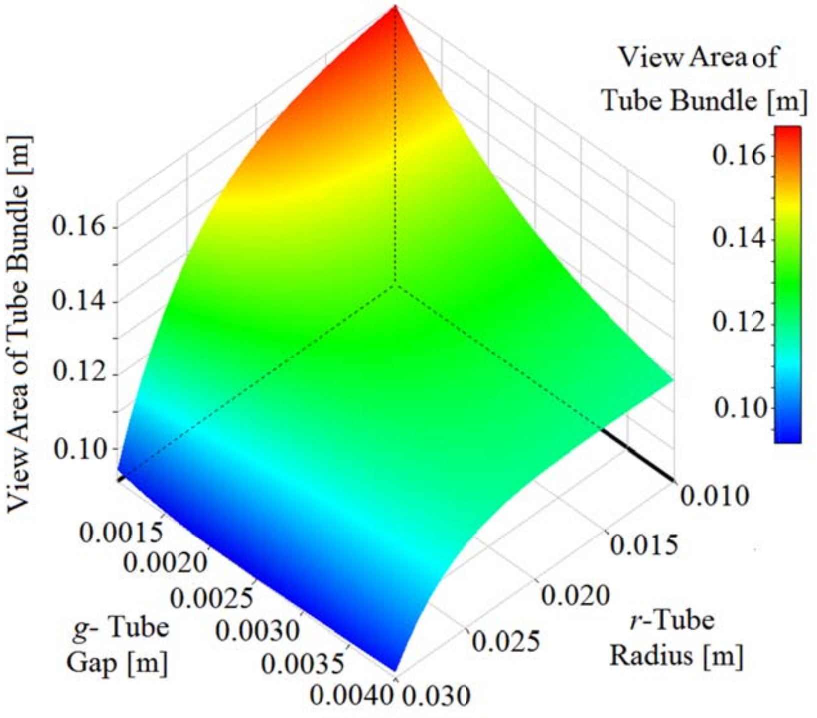
View Area of Tube Bundle [m]
0.16
0.14
0.12
0.10
View Area of Tube Bundle [m]
0.16
0.14
0.12
0.10
0.0015
0.0020
0.0025
0.0030
0.0035
0.0040
g- Tube Gap [m]
0.030
0.025
0.020
0.015
0.010
r-Tube Radius [m]

(b)

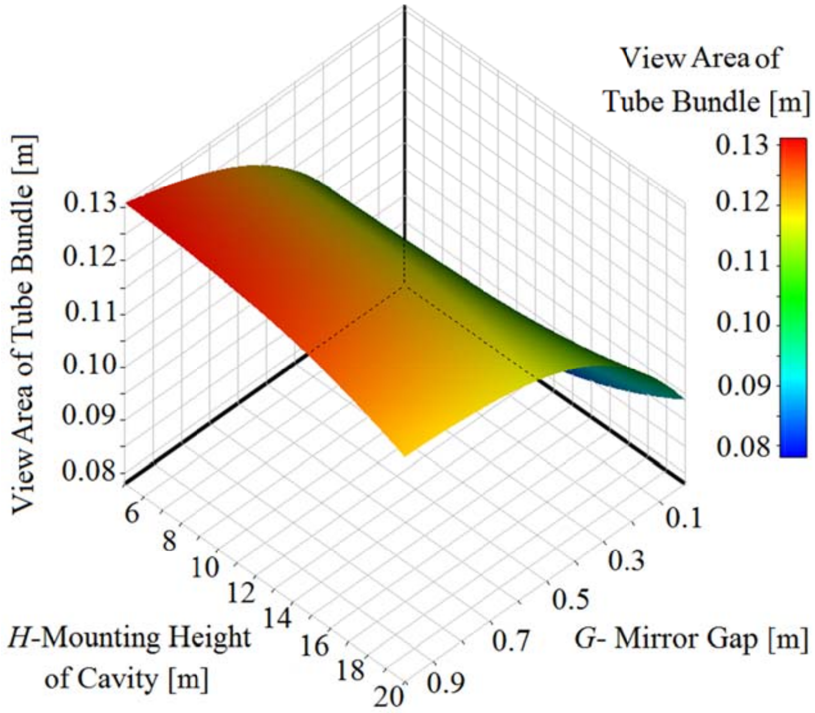

(c)

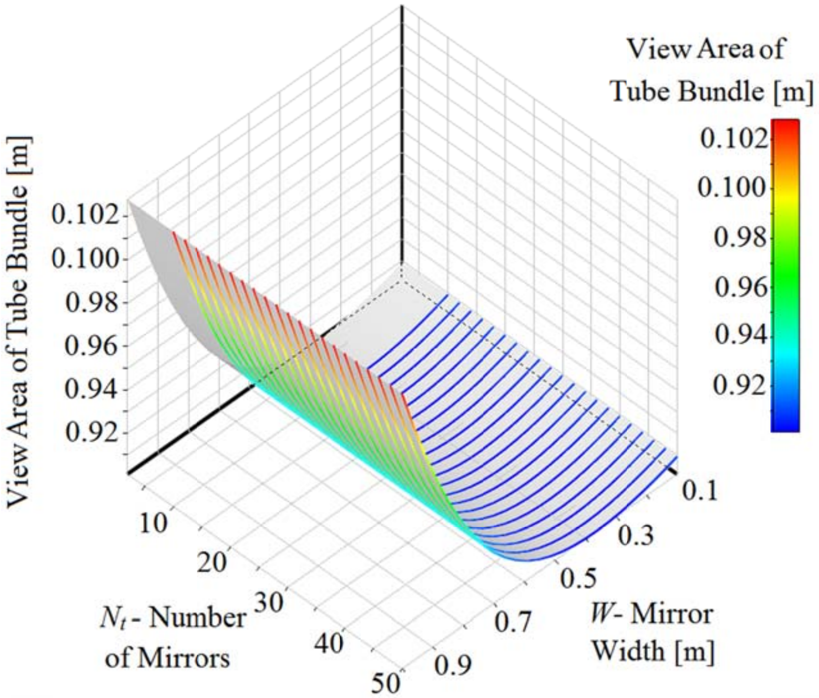

(d)

Fig. 11. Response surfaces of the View Area of Tube Bundle vs. independent parameters. a) View area of tube bundle vs. cavity depth and cavity angle. b) View area of tube bundle vs. tube gap and tube radius. c) View area of tube bundle vs. mounting height of cavity and mirror gap. d) View area of tube bundle vs. number of mirrors and mirror width.

Finally, Fig. 12 shows the effect of the optimisation-independent parameters on the daily solar power objective. Fig. 12-a depicts the effect of cavity depth and cavity angle on daily solar power. A decrease in cavity angle or increase in cavity depth would lead to fewer tubes fitting into the cavity, which means that fewer reflected rays from the mirror field would hit the absorber tubes or that the absorbed solar power throughout a day would decrease. Fig. 12-b displays the effects of the tube radius and the tube gap on daily solar power. Increasing the tube gap parameter means that the tubes are situated further from each other in the cavity, which leads to more reflected rays hitting the absorber tubes. This would increase the absorbed daily solar power, which is shown in this figure. In addition, for a specific tube gap, by increasing tube radius, the absorbed daily solar power drops. Indeed, increasing the tube radius would lead to fewer tubes in the tube bundle due to insufficient fitting space in the cavity and consequently less rays hit the absorber tubes. Fig. 12-c shows the effects of mirror gap and the mounting height of the cavity on daily solar power. As displayed, by increasing the mounting height of the cavity, the daily solar power increases. Actually, increasing the mounting height of the cavity leads to less blocking and shading in the mirror field. In addition, for a specific mounting height of the cavity, decreasing the mirror gap leads to compactness of mirror field. Although the field compactness increases the blocking and shading effects of the mirror field, due to a fixed aperture assumption, this fact would also let more mirrors play a role in solar ray concentration on the tube bundle throughout a day. This leads to increasing the daily solar power by reducing the mirror gap. Fig. 12-d displays the effect of the number of mirrors and the mirror width on the daily solar power. The response surface shows by adding more mirrors or by increasing the mirror width the daily solar power increases. This is to be expected, since, increasing those independent parameters leads to increasing the mirror field reflected area which consequently leads to more solar rays impinging on the absorber tubes.

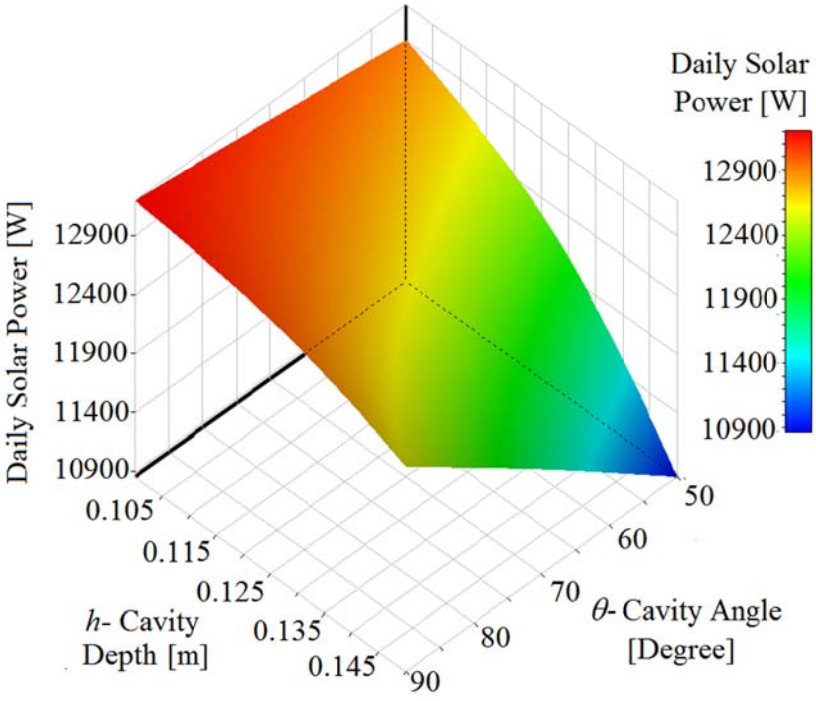

(a)

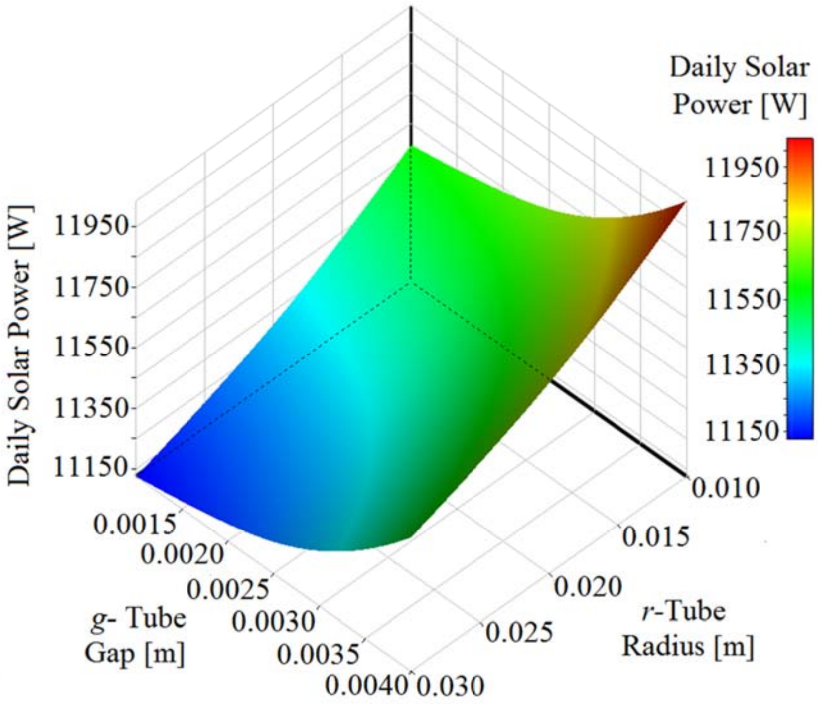
Daily Solar Power [W]
11950
11750
11550
11350
11150
Daily Solar Power [W]
11950
11750
11550
11350
11150
0.0015
0.0020
0.0025
0.0030
0.0035
0.0040
g- Tube Gap [m]
0.010
0.015
0.020
0.025
0.030
r-Tube Radius [m]

(b)

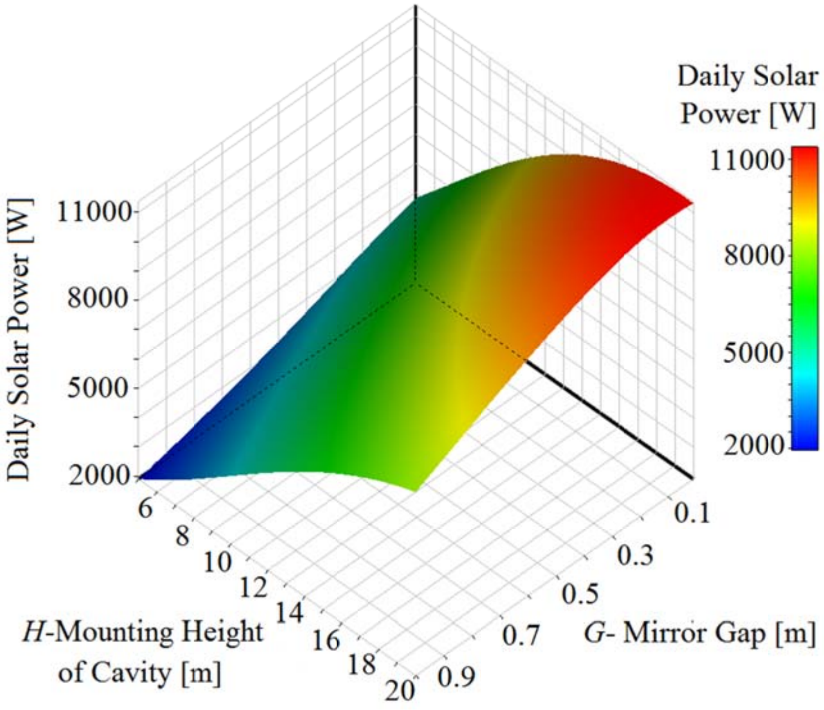
Daily Solar Power [W]
11000
8000
5000
2000
Daily Solar Power [W]
11000
8000
5000
2000
6
8
10
12
14
16
18
20
H-Mounting Height of Cavity [m]
0.1
0.3
0.5
0.7
0.9
G- Mirror Gap [m]

(c)

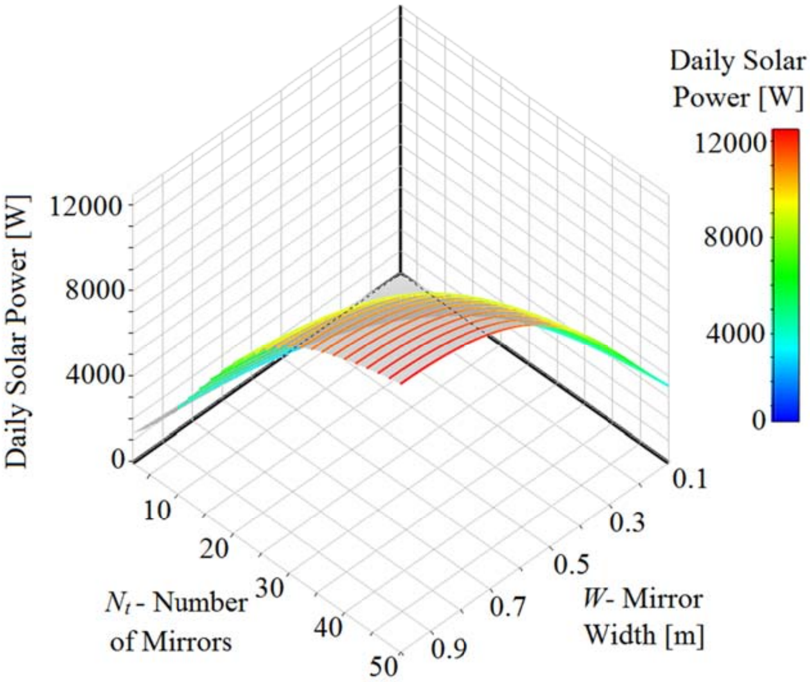

(d)

Fig. 12. Response surfaces of Daily Solar Power vs. independent parameters. a) Daily solar power vs. cavity depth and cavity angle. b) Daily solar power vs. tube gap and tube radius. c) Daily solar power vs. mounting height of cavity and mirror gap. d) Daily solar power vs. number of mirrors and mirror width.

Lastly, the values of three utopian designs were automatically chosen by ANSYS DX among all the feasible Pareto optimal cases and reported as candidate points. The suggested utopian points based on the response surface optimisation are reported in Table 11. These parameter combinations were re-calculated using Excel and SolTrace to provide the "calculated" values in the table. There is a difference between the predicted and verified calculated values, but the latter should be used as it is based on a simulation and not on a response surface prediction.

Cavity depth and cavity angle parameters in all candidates tend towards maximum and minimum bounds, respectively. Actually, this driving to extreme bounds tries to move the cavity receiver to its deepest and most acute-angled case. According to what has been discussed, this physically make sense, since the deepest and most acute-angled case trapped appropriate amount of solar rays (increasing solar power on the tube bundle), while these two parameters decrease the available cavity rooms for placing the tube bundles (decreasing the number of tubes), which has a great effect on reducing the cavity's economic cost and the view area of the tube bundle. Therefore, these two parameters tend towards their extremes since they could satisfy all optimisation objectives. However, the rest of the parameters are unconstrained at the optimum candidates.

Table 11
Candidate utopian points

Parameters [unit]	First candidate	Second candidate	Third candidate	Chosen feasible optimum case
Number of mirrors – N_m	38	34	48	38
Mirror width – W [mm]	681.424	684.156	683.963	681

Mirror gap – G [mm]	22.837	13.667	31.347	23
Mounting height of cavity – H [m]	18.60455	18.40368	18.60455	18.605
Tube radius – r (tube outer diameter – OD) [mm]	29.235 (58.47)	29.245 (58.49)	29.235 (58.47)	30.165 (60.33)
Tube gap – g [mm]	2.996	3.795	2.981	2
Tube bundle offset from cavity top wall – d [mm]	38.783	38.74	38.783	39
Cavity angle – θ [degree]	51.09491	52.18280	51.09173	51
Cavity depth – h [mm]	143.586	142.866	143.976	144
Optimisation objective	**Predicted (calculated)**	**Predicted (calculated)**	**Predicted (calculated)**	
View area of tube bundle [m]	0.099131 (0.116163)	0.106272 (0.116705)	0.099179 (0.116052)	0.119556
$\gamma_{\mathit{Plant\ Cost\ Factor}}$	2 441.743 (2 449.281)	2 263.142 (2 237.124)	2 990.202 (2 999.153)	2 459.952
Daily solar power [W]	11342.85 (13 113.3)	11090.60 (12 204.59)	12232.17 (14 644.5)	13 161.23

Due to the prediction of output goals, the first point candidate was suggested as the final result for further investigation. However, it should be considered that, although those inlet parameter values might mathematically lead to optimum results, it would not be practical to fabricate such a collector due to the existence of manufacturing limitations or material availability. For instance, any mathematical tube's outer diameter that was calculated in the optimisation process is not available in the market. According to Table 12, the closest available industrial pipe that could be purchased has a 60.33 mm outer diameter. The internal tube diameter (ID) is related to the OD and the schedule of the tube. The latter determines the tube wall thickness as governed by the operating pressure and pressure drop due to the friction losses of the plant. As the analysis methods used in this study focus on external tube surface factors (optics or heat absorption and heat losses) and not on the heat transfer fluid performance as governed by the ID, the OD is used as design parameter. In general, due to manufacturing and procurement limitations (i.e. cutting, bending, welding and manufacturing processes' tolerances, as well as material availability in the market), the values of the first-point candidate parameters have to be adjusted to feasible values. Such data have been reported under the chosen feasible optimum case column in Table 11.

Table 12
Industrial pipes close to 56 mm OD (TPS, 2016; Industrial Business Link, 2016).

Nominal Pipe Size (NPS)	**Nominal diameter (DN)**	**OD [in (mm)]**
1 1/4	32	1.660 (42.16)
1 1/2	40	1.900 (48.26)
2	50	2.375 (60.33)
2 1/2	65	2.875 (73.03)
3	80	3.500 (88.90)

Finally, the determined optimisation objectives were recalculated for the optimum case as reported in Table 11. In the process, the output daily solar power curve was determined as shown in Fig. 15, to be discussed later. The final configuration of the optimum collector case is displayed in Fig. 13. The variation in focal length is shown in the figure to provide context for the next section.

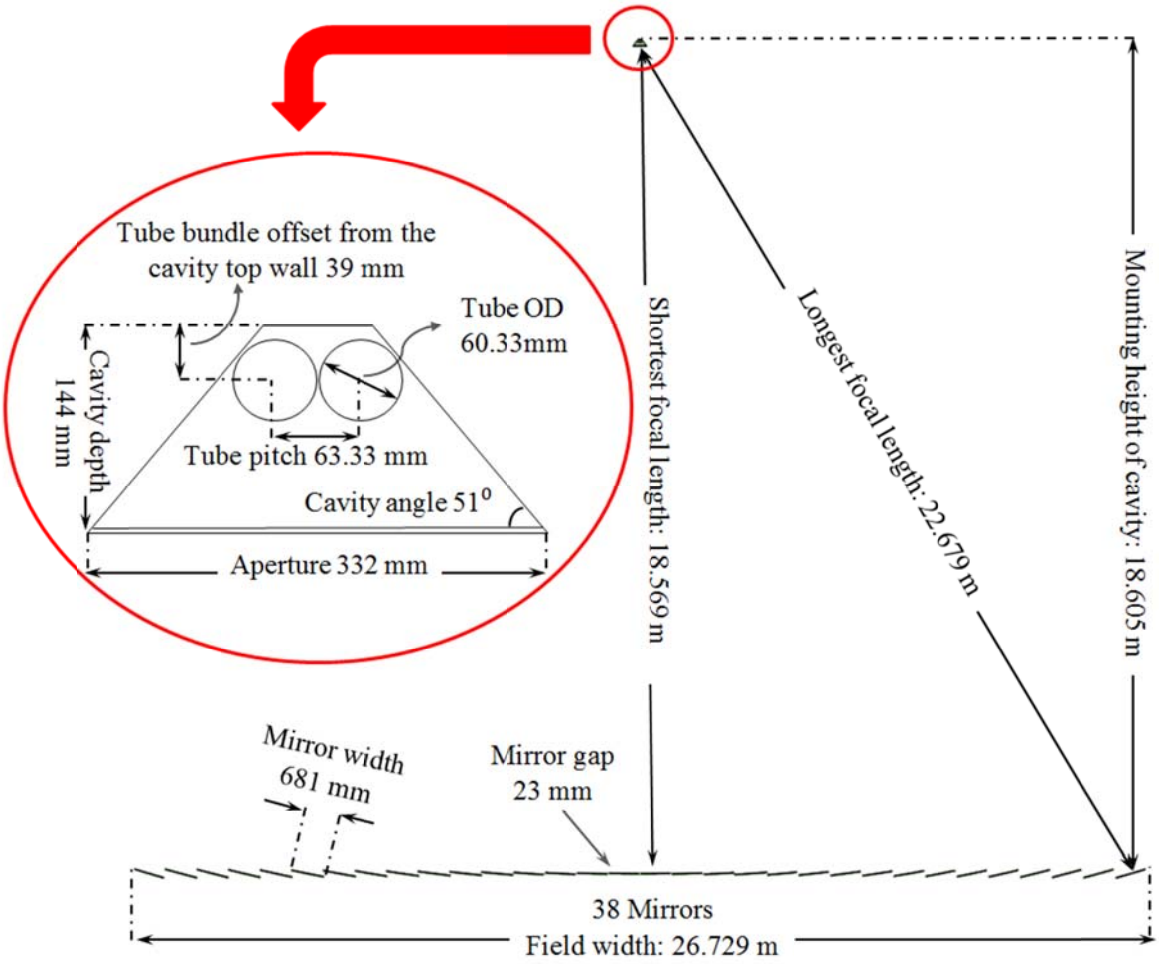

Fig. 13. Configuration of the optimum LFC collector is displayed at 12 noon.

The optimisation process resulted in an ideal feasible optimum collector, where each individual mirror has a unique focal length. Theoretically, considering individual mirror focal lengths across the mirror field might seem beneficial since it leads to better solar ray concentrations on the cavity tube bundle (higher solar output), whereas, in practice, it might be impractical, since the manufacturing process, assembly and maintenance process of the collector gets more complicated. For example, the proposed optimum case requires 32 mirrors rows, which means that at least 16 mirror manufacturing lines are needed to bend the mirrors properly and provide the required focal lengths, or 16 storage lines have to be considered for mirror spare parts. As a consequence, the process of mirror maintenance and collector assembly is complex. In addition to the complexity, this increases the final cost of the mirror field. Unfortunately, there is not an available economic model to check how the complexity of the mirror field affects the economic cost of a field. However, it is possible to check the optical penalty of using a single focal length for the proposed optimum collector domain. Therefore, a supplementary optimisation study is performed to improve the practicality of the proposed optimum ideal collector. In this study, an optical optimisation investigates the optimum fixed focal length for the entire proposed collector. It should be noted that only a typical summer day is considered in this study. A more representative annual performance is outside the scope of this paper but can be contained by constructing a total solar power based on a seasonal variation in the solar angle (down to almost 45° in winter) and then finding the fixed focal length that maximises annual performance.

The optimisation process, tools and loop in this study are the same as that described in section 3.1.1 and Fig. 7. However, instead of defining a set of design variables in the optimisation of multi-objective goals, only one independent variable (focal length) and one goal (daily solar power) is considered with the other variable held fixed at the values determined above. A focal length range of 10 to 50 m was allowed in the optimisation.

The optimisation converged after 618 iterations on the Kriging response surface when considering the default importance for the daily solar power objective. The result of this single optimisation process is shown in Fig. 14. A single maximum is observed at a focal length of 24 m.

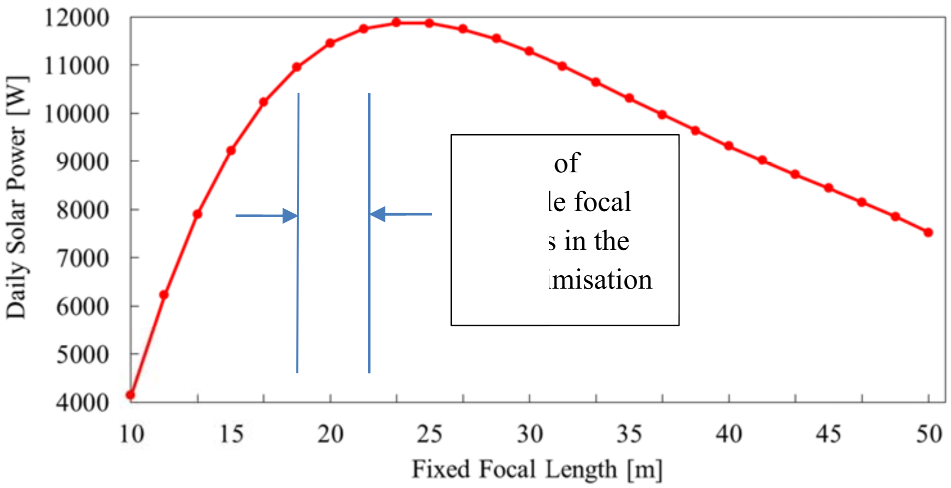

Fig. 14. Response curve of independent variable vs. daily solar power

According to Fig. 13, at a focal length of 24 m, all the mirrors across the field concentrate their reflected rays at the optimum point *beyond* the tube bundle. This means that the tube bundle truncates the reflected rays from a mirror before the convergence of rays at a point. In other words, instead of point concentration rays on a point in the cavity, an optimum region of the tube bundle is hit by rays from each mirror (due to the truncation of the ray concentration cone). This leads to the optimum harvested solar power on the tube bundle for this study (see Fig. 14).

Finally, the trends of total solar incident power on absorber tubes for both the fixed optimum focal length case and the case of individual focal lengths are displayed in Fig. 15, confirming the compromise in total power as a result of the practical single focal length implementation.

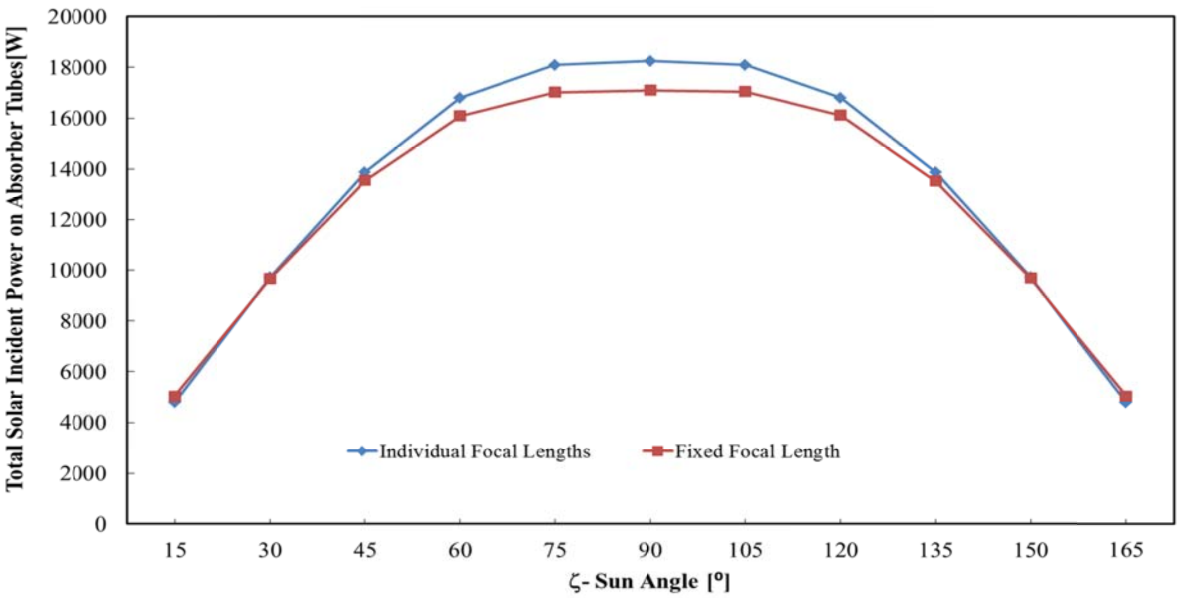

Fig. 15. The curve of total solar incident power on absorber tubes for both fixed and individual focal length cases throughout a day.

The interesting fact in Fig. 15 is the reduction of the magnitude of daily solar power for the optimum collector from 13 161.23 (W) to 12 713.3 (W) for the fixed focal length case (3.4%). It is an expected phenomenon, since by using a single focal length for the entire mirror field, the mirrors defocus much more than in the case where each individual mirror focuses perfectly on the cavity receiver. This is the penalty imposed on designing a much simpler and more practical LFC. However, for better judgment on the penalty of a fixed focal length a comprehensive annual performance of total solar power based on a seasonal variation of solar angle, has to be performed which can be studied in future by researchers. Such a study would also determine what fixed focal length would lead to the best annual performance.

4.2. Optimisation results for the second problem (insulation optimisation for the proposed optimum cavity)

As displayed schematically in Fig. 8, the cavity arrangement of the optimum collector case is obtained. However, the optimum insulation of this optimum cavity would find a balance between thermal heat losses from the cavity and the cost of the required insulation. Therefore, in this section, the results of the cavity insulation optimisation are presented. The optimisation problem was discussed in section 3.1.2. The optimisation converged after 138 iterations when considering a higher importance for the heat loss objective and a default importance for the insulation area objective. The effect of independent parameters on optimisation objectives is presented in Fig. 16. This figure is displayed for the introduced independent parameters in the feasible case column in Table 13. In this figure, the independent parameters are held constant at their optimum values when not plotted in a particular sub-figure. The effects of the side and top insulation thicknesses on the insulation area and heat loss objectives are shown in Fig. 16-a and Fig. 16-b, respectively. Increasing both the side and top insulation thicknesses increases the insulation area and consequently insulation cost, while the heat loss from the cavity is reduced as expected (the response surface moves to less negative values, which means improved insulation). In Fig. 16-c, the effect of the third independent parameter of this optimisation (top insulation angle) on the insulation area and on heat loss are depicted, respectively. By increasing this angle, the insulation area increases. This is the expected effect and can be physically justified due to its definition. Indeed, by increasing this parameter, the top insulation shape transforms from a trapezoidal shape to a rectangular shape. The nonlinear behaviour of the top insulation angle trend on heat loss is due to the singularity (sharp point in the physical shape) of the cavity's top corners, which is displayed in Fig. 16-c. A similar behaviour was observed in Moghimi et al. (2015c). As displayed in this figure, by increasing the angle, the heat loss decreases.

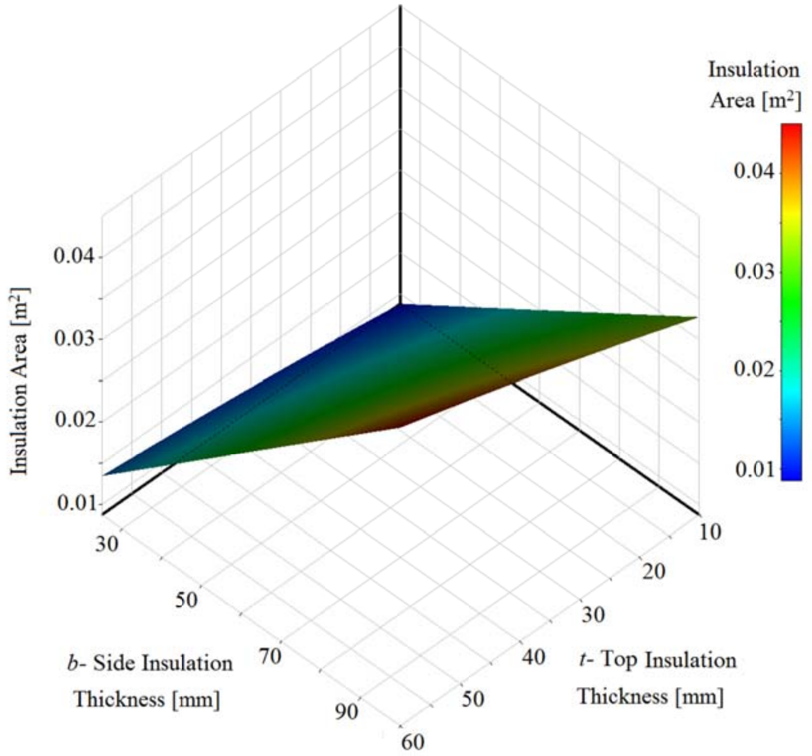

(a)

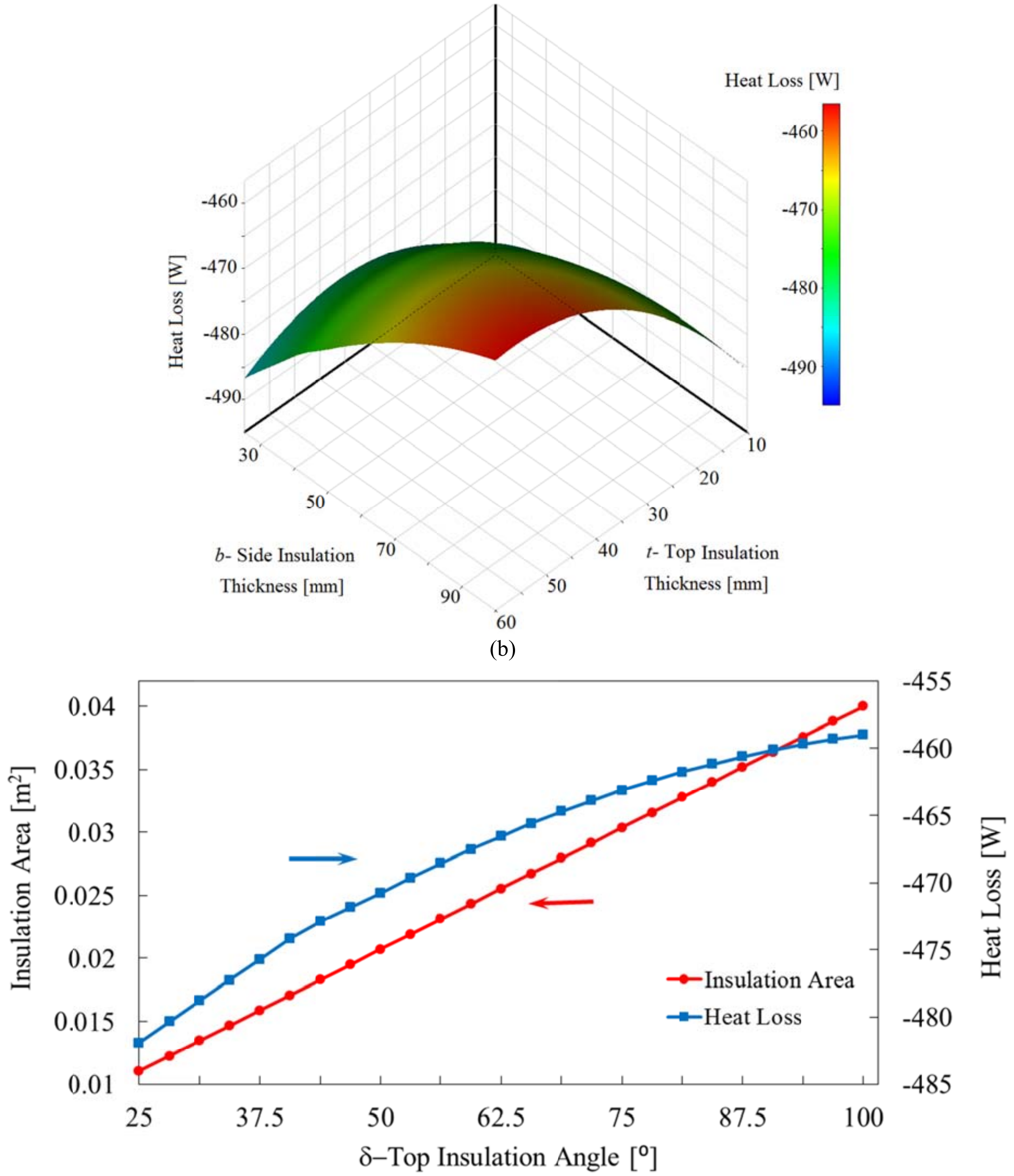

(b)

(c)

Fig. 16. Response surfaces of objective goals vs. independent parameters. a) Insulation area vs. side and top insulation thickness. b) Heat loss vs. side and top insulation thickness. c) Insulation area and heat loss vs. top insulation angle.

Finally, ANSYS DX reported values of three utopian points among all feasible Pareto optimal cases. Before further discussion of these utopian points, it has to be considered that the above observations are based on a temperature of 500 K in the tube bundle in the cavity, while in an LFC plant, the tube bundle temperature increases steadily across the plant length, depending on pipe routing, heat transfer fluid type, etc. Therefore, the optimal insulation layout could be different for different parts of the plant, based on the local tube bundle temperature. As an attempt to address this issue, the optimisation process was replicated for two more tube bundle temperatures of 300 K and 400 K. The utopian points for all suggested temperatures (including 500 K) are tabulated in Table 13.

Because of the similarity in heat loss performance of the suggested points at a certain temperature, as well as the practicality considerations and reducing the complexity of plant control, it is conceivable to pick one insulation configuration for the whole plant. Therefore, the candidate with the minimum insulation area (the first candidate for the 500 K case) was selected for further study. However, due to manufacturing limitations, the candidate parameters were rounded off to feasible values as reported in the feasible case column in Table 13.

Finally, the CFD simulation was repeated for the feasible case and insulation area. The heat loss results are reported in Table 13 and Fig. 17. In addition, Fig. 17 displays the detailed CFD results of the proposed cavity with optimum insulation, evaluated at a tube temperature of 350 K and 500 K. The figure is depicted in the form of temperature contours overlaid with velocity vectors due to natural convection at different stages of a plant (350 K and 500 K tube temperature) under two different atmospheric conditions. In this figure the effect of the atmospheric condition was simulated by changing the convective coefficient in the CFD simulations. The heat loss contributions from the different external boundaries are also displayed in Fig. 17. As shown, by increasing the tube bundle temperature, the heat loss increases significantly due to the dominance of the radiation heat loss mechanism. This fact can also be seen in the contribution of re-radiation from the glass cover in comparison to the other heat loss from other boundaries. This proves the claim of section 2.4.2 about the dominance of the radiation mechanism heat loss. In addition, the negative slope stratification of temperature leads to low velocity in the lower part of the cavity and higher velocity close to the tubes, thereby reducing internal convection loss. This behaviour was also observed in Moghimi et al. (2015c). In addition, the velocity of the natural convective fluid flow is influenced more by the tube bundle temperature than by the atmospheric conditions, which is a physically expected phenomenon since the tube bundle temperature difference with environmental temperature is the main driver of the natural convection phenomenon. Hence, a higher tube bundle temperature has higher velocity magnitudes.

Last, but not least, the accuracy of the suggested view area approach in this paper is investigated. The heat loss calculation via the view area approach is computed by means of Eq. (26). This heat loss calculation is reported per unit length as:

$$q_{heatloss} = \sigma \varepsilon_{Tubebundle} A\left(T_{Tubebundle}^{4} - T_{Mirror\ field}^{4}\right) \tag{26}$$

where σ is the Stefan-Boltzmann constant, $\varepsilon_{Tubebundle}$ is the emissivity of the tube bundle (see Table 5), A is the view area of the tube bundle per unit length (see the objective of the feasible optimum case in Table 11), $T_{Tubebundle}$ is the tube bundle temperature and $T_{Mirror\ field}$ is the temperature of the mirror field (305 K, see Table 5). Fig. 18 shows how accurate this approach could be in the heat loss prediction of an LFC plant. At 500 K, this approach undershoots the CFD result of the glass heat loss with no wind (convective heat transfer coefficient equal to 0 W/m^{2}K) by 0.87%. The other CFD curves show the total heat loss from the cavity, as well as the heat transfer from all boundaries *except* the glass. Because of the dominance of the radiation mechanism, the glass radiation heat loss follows a similar trend to the total heat loss, with the view area approach underpredicting the total heat loss at 500 K by17.5%. The authors admit that the view area approach is not as accurate as a CFD simulation for the thermal modelling of an LFC plant. However, in order to speed up the expensive process of optimisation, it could be a useful alternate approach for a quick estimate of total heat loss.

Table 13
Candidate utopian points

	Tube temperature at 300 K			Tube temperature at 400 K			Tube temperature at 500 K			
Parameters [unit]	**First candidate**	**Second candidate**	**Third candidate**	**First candidate**	**Second candidate**	**Third candidate**	**First candidate**	**Second candidate**	**Third candidate**	**Feasible case**
Top insulation angle – δ [degree]	40.49	42.78319	88.73331	73.40938	43.26054	82.63	82.63	88.10921	41.76734	42
Top insulation thickness – t [mm]	12.325	30.18043	57.02018	52.09626	46.32552	51.90625	51.90625	48.60084	42.53125	43
Side insulation thickness – b [mm]	25.75	26.99304	95.82887	67.73623	56.30555	71.12037	71.12037	66.29728	56.61946	57
Optimisation objective	**Predicted (Calculated)**	**Predicted (Calculated)**	**Predicted (Calculated)**	**Predicted (Calculated)**	**Predicted (Calculated)**	**Predicted (Calculated)**	**Predicted (Calculated)**	**Predicted (Calculated)**	**Predicted (Calculated)**	**Calculated**
Heat loss from boundaries [W]	-5.1398 (-7.04248)	-5.07964 (-6.5023)	-4.60396 (-5.01997)	-163.628 (-163.476)	-166.6436 (-166.861)	-162.921 (-162.987)	-460.18 (-460.54)	-462.29 (-462.607)	-468.474 (-469.425)	See Fig. 17
Insulation area [m^2]	0.037998 (0.037998)	0.03523 (0.03523)	0.027441 (0.027441)	0.035739 (0.035739)	0.027449 (0.027449)	0.037998 (0.037998)	0.011667 (0.011667)	0.012397 (0.012397)	0.052577 (0.052577)	0.0276645

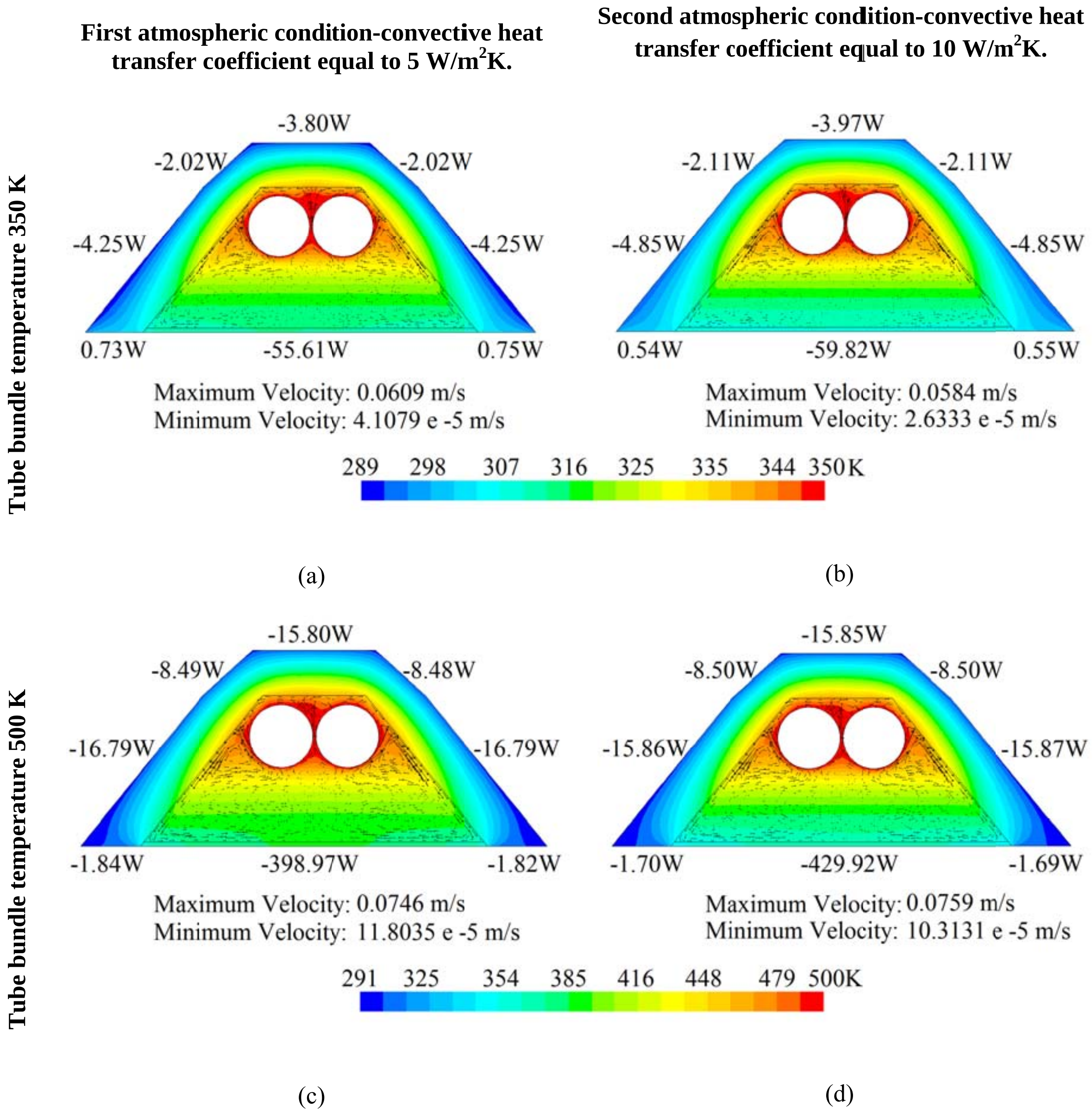

(a) (b)

(c) (d)

Fig. 17. CFD Temperature contours overlaid with velocity vectors for the cavity optimum case under different convective conditions and different Tube Bundle temperature. a) under first atmospheric condition with tube bundle temperature 350K. b) under second atmospheric condition with tube bundle temperature 350K. c) under first atmospheric condition with tube bundle temperature 500K. d) under second atmospheric condition with tube bundle temperature 500K.

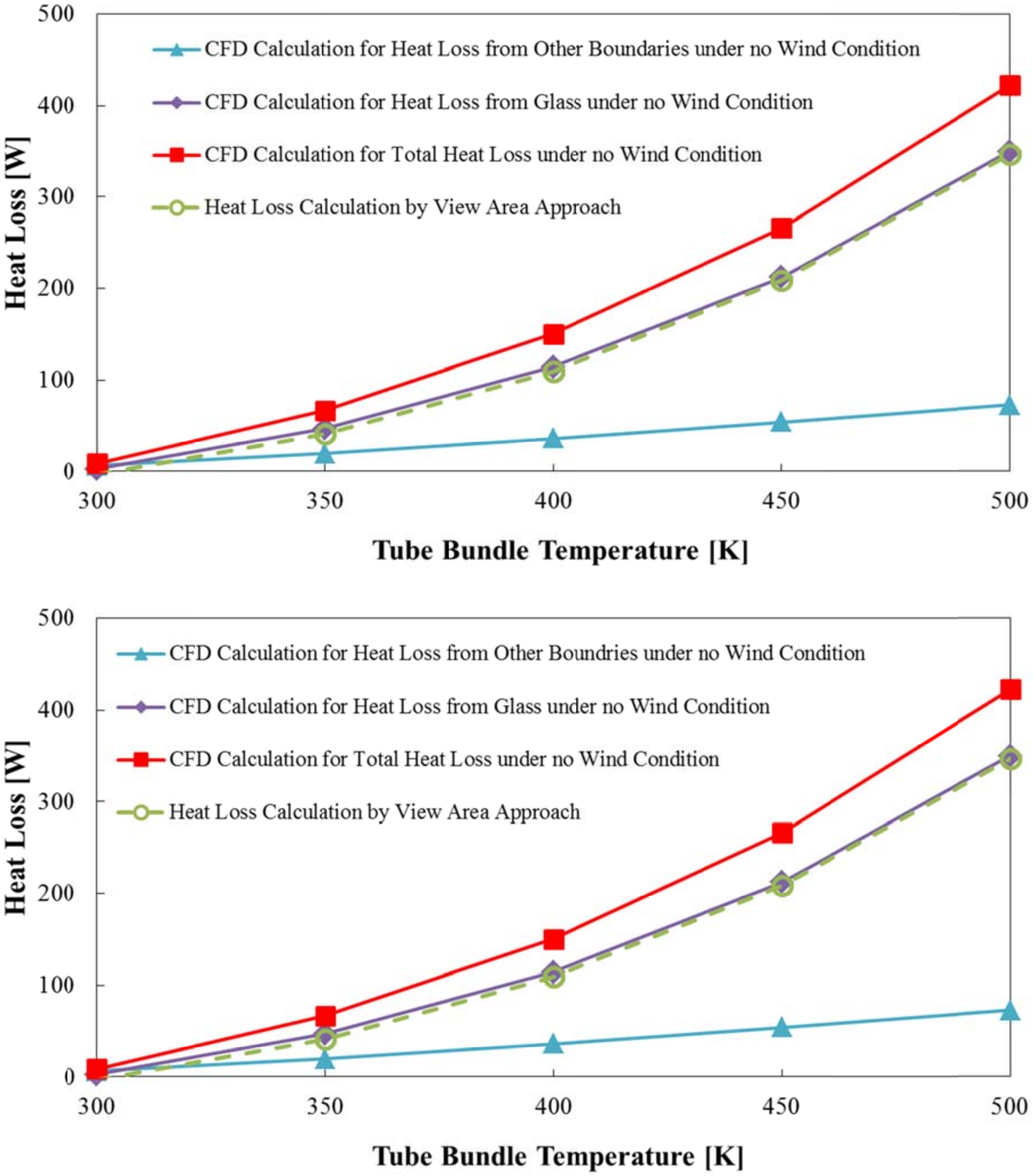

Fig. 18. Heat loss comparison of CFD and view area approach for no wind condition.

5. Conclusion

Mathematical optimisation is a powerful tool to help reach engineering optimisation goals. In this paper, the optimisation of an LFC with a multi-tube trapezoidal cavity configuration was addressed through a two-phase series optimisation process in order to find the most appropriate collector with minimum constructional cost and expense, highest solar absorption power throughout a day, as well as minimum heat loss. The first goal led to the economic optimisation of a collector (cheap solar electricity generation from an LFC plant), while the other goals resulted in a more optically and thermally efficient collector, respectively (harvesting more solar energy throughout a day). The multiple objectives were incorporated using a multi-objective genetic algorithm to find multiple Pareto optima. If all competing objectives are not included in a design formulation, one objective might be optimised at the expense of other performance parameters. Some specific conclusions can be made regarding the work:

1. The careful selection of geometrical parameters and splitting them into two groups that govern the geometry of collector and insulation allows the design optimisation process the freedom to suggest candidate optimum designs to fulfil the objectives in a quick and reasonable approach. In a departure from previous LFC cavity optimisation that studied a fixed number of tubes, the current paper treated the tube number as a variable. Interestingly, the optimal design led to a cavity with only two tubes, as a trade-off was found between cavity cost, optical performance and heat loss. Mirror gap, mirror length, cavity height, cavity depth, number of mirrors all reached optimal values somewhere in the allowable bands. Only the tube radius (maximum), gap between tubes (minimum) and cavity angle (minimum) reached one of their bounds. The latter three parameters had the consequence of only two tubes being optimal.

2. Letting each LFC mirror have a unique manufacturing curvature as determined by its distance to the centre of the cavity provided the highest optical performance. A more practical alternative was investigated by performing an optimisation of an ideal fixed mirror curvature. Interestingly, a curvature *beyond* the cavity centroid was found. This configuration only resulted in a 3.4% reduction compared to the more complicated and less practical case - individually curved mirrors.

3. Heat loss estimation with reasonable accuracy and computational effort speeds up the calculation process of thermal modelling. This is one of the essential requirements for such a comprehensive optimisation study to run the simulation in a reasonable time frame and assess the relative importance in the optimisation process. The traditional use of the CFD simulation has been replaced with a quicker approach with reasonable accuracy in the optical and thermal economic optimisation phase. The approach was called the view area approach, which is based on this fact that the most dominant mechanism in heat loss from an LFC cavity is radiation heat transfer. In this approach, the tube bundle temperature was taken as the main driver of the radiative heat loss mechanism, and the portion of its area, which participates in radiation to the mirror field, was determined as the view area. The approach consistently underpredicts the total heat loss because it neglects other heat loss mechanisms than radiation. This approach was however proved to have a reasonable accuracy, coupled with a large reduction in computational effort.

4. With the help of the view area approach, the thermal objective goal of the collector optimisation was independent from a CFD calculation. This fact led to the suggestion

of a series two-phase optimisation approach. In the first phase, the collector domain went through a thermal, optical and economic optimisation study, while the second phase used the results of the first phase to find the thermal and economic optimal insulation around the proposed cavity. This series approach sped up the process of optimisation by reducing the number of independent parameters in each phase, as well as reducing the complexity of the simulation.

5. A limited investigation of varying the specified tube bundle temperature was performed for the insulation optimisation to mimic the fact that an LFC cavity receiver would be operating at different temperatures, depending on the location along the length of the plant. Here, the radiation mechanism was again proven to be dominant, while natural convection velocities in the cavity were increased with increasing tube bundle temperatures.

Acknowledgements

The authors would like to acknowledge the support of the University of Pretoria (South Africa) and the South African National Research Foundation (DST-NRF Solar Spoke).

References

Abbas, R., Munoz-Anton, J., Valdes, M., Martinez-Val, J., 2013. High-concentration linear Fresnel reflectors. *Energy Convers. Manage.* 72, 60-68. In: the 3rd International Conference on Nuclear and Renewable Energy Resources {NURER2012}.

Abbas, R., Montes, M.J., Rovira, A., Martinez-Val, J.M., 2016. Parabolic trough collector or linear Fresnel collector? A comparison of optical features including thermal quality based on commercial solutions, Solar Energy 124 198–215.

Areva, 2016. Areva Solar. Available from http://www.areva.com/EN/solar-220/arevasolar.html.

Ansys, 2013. Ansys Fluent Help, version 15, ANSYS Incorporated.

Bernhard, R., Laabs, H.G., de Lalaing, J., Eck, M., Eickhoff, M., Pottler, K., Morin, G., Heimsath, A., Georg, A., Häberle, A., 2008. Linear Fresnel collector demonstration on the PSA Part I – design: construction and quality control. In: Presented at the 15th SolarPACES International Symposium, Berlin, Germany.

Cengel, Y.A., Ghajar, A. J., 2010. Heat and mass transfer fundamentals and applications, 4th edition, McGraw-Hill.

Craig, K.J., Moghimi, M.A., Rungasamy, A.E., Marsberg, J., Meyer, J.P., 2016. Finite-volume ray tracing using Computational Fluid Dynamics in linear focus CSP applications. *Appl. Energy* 183, 241-256.

Conlon, W.M., 2011. Superheated steam from CLFR solar steam. In: Presented at the 17th SolarPACES International Symposium, Granada, Spain.

Dey, C.J., 2004. Heat transfer aspects of an elevated linear absorber. *Sol. Energy* 76, 243-249.

Facão, J., Oliveira, A.C., 2011. Numerical simulation of a trapezoidal cavity receiver for a linear Fresnel solar collector concentrator. *Renew.Energy* 36, 90- 96.

Flores Larsen, S., Altamirano, M., Hernández, A., 2012. Heat loss of a trapezoidal cavity absorber for a linear Fresnel reflecting solar concentrator. *Renew. Energy* 39, 186-206.

Government of Spain, 2012. Royal Decree Law 1/2012, *Boletín Oficial del Estado*. Available from http://www.boe.es/boe/dias/2012/01/28/pdfs/BOE-A-2012-1310.pdf.

Günther, M., 2017. Linear Fresnel Technology, *Enermena; Deutsches Zentrum fur Luft- und Raumfahrt.* Available from http://www.energy-science.org/bibliotheque/cours/1361468614Chapter%2006%20Fresnel.pdf

Haberle, A., Zahler, C., Lerchenmuller, H., Mertins, M., Wittwer, C., Trieb, F., Dersch, J., 2002. The solarmundo line focussing Fresnel collector: optical and thermal performance and cost calculations. In: Presented at11th SolarPACES International Symposium,, Zurich, Switzerland.

Heimsath, A., Cuevas, F., Hofer, A., Nitz, P., Platzer, W., 2014. Linear Fresnel collector receiver: heat loss and temperatures. Energy Proc. 49 (0), 386-397, Proceedings of the SolarPACES 2013 International Conference.

Hongn, M., Larsen, S.F., Gea, M., Altamirano, M., 2015. Least square based method for the estimation of the optical end loss of linear Fresnel concentrators. *Sol. Energy* 111, 264-276.

Industrial Business Link, 2016. Standard pipe schedule and inner diameter. Available from http://iblink.com.pk/Links-data/Free-gifts/2_PIPE%20SCHEDULE%20&%20INNER%20DIA%20DIMENSIONS.pdf.

Jance, M.J., Morrison, G.L., Behnia, M., 2000. Natural convection and radiation within an enclosed inverted absorber cavity: preliminary experimental results. In: Presented at the 38th ANZSES conference, Brisbane Australia.

Lai, Y., Wu, T., Che, S.H., Dong, Z., Lyu, M., 2013. Thermal performance prediction of a trapezoidal cavity absorber for a linear Fresnel reflector. *Advances in Mechanical Engineering*. Available from http://dx.doi.org/10.1155/2013/615742.

Lienhard IV, J.H., Lienhard V, J.H., 2003. A heat transfer textbook, 3rd edition. Cambridge, MA: Phlogiston Press.

Manikumar, R., Valan Arasu, A., Jayaraj, S., 2014. Numerical simulation of a trapezoidal cavity absorber in the linear Fresnel reflector solar concentrator system. *Int. J. Green Energy* 11, 344-363.

Mertins, M., 2009. Technische und wirtschaftliche analyse von horizontalen Fresnel-kollektoren, PhD thesis, University of Karlsruhe. In German.

Moghimi, M.A., 2017. Optical, thermal and economic optimization of a Linear Fresnel Collector. PhD thesis, University of Pretoria.

Moghimi, M.A., Craig, K.J., Meyer, J.P., 2014. Optimization of a trapezoidal cavity absorber for the linear Fresnel reflector. In: Presented at the 2nd SASEC, Port Elizabeth, South Africa.

Moghimi, M.A., Rungasamy, A., Craig, K.J., Meyer, J.P., 2015a. Introducing CFD in the optical simulation of linear Fresnel collectors. In: Presented at the 21th SolarPACES International Symposium, Cape Town, South Africa.

Moghimi, M.A., Craig, K.J., Meyer, J.P., 2015b. A novel computational approach to the combine optical and thermal modeling of a linear Fresnel collector receiver. In: Presented at the 3rd SASEC, Kruger National Park, South Africa.

Moghimi, M.A., Craig, K.J., Meyer, J.P., 2015c. Optimization of a trapezoidal cavity absorber for the Linear Fresnel Reflector. *Sol. Energy* 119, 343-361.

Moghimi, M.A., Craig, K.J., Meyer, J.P., 2015d. A novel computational approach to combine the optical and thermal modelling of linear Fresnel collectors using the Finite Volume Method. *Sol. Energy* 116, 407-427.

Montes, M.J., Abbas, R., Rovira, A., Martinez-Val, J.M., Muñoz-Antón, J., 2012. Analysis of linear Fresnel collectors designs to minimize optical and geometrical losses, In: Presented at the 18th SolarPACES International Symposium, Marrakech, Morocco.

Morin, G., Platzer, W., Eck, M., Uhlig, R., Haberle, A., Berger, M., et al., 2006. Road map towards the demonstration of a linear Fresnel collector using a single tube receiver. In: Presented at the 13th SolarPACES International Symposium, Las Vegas, NV, United States.

Natarajan, S.K., Reddy, K.S., Mallick, T.K., 2012. Heat loss characteristics of trapezoidal cavity receiver for solar linear concentrating system. *Appl. Energy* 93, 523-531.

National Renewable Energy Laboratory (NREL), 2016. Linear Fresnel reflector projects. Available from http://www.nrel.gov/csp/solarpaces/linear_fresnel.cfm.

Novatec Solar, 2016. About Novatec Solar. Available from http://www.novatecsolar.com/.

Pye, J.D, Morrison, G., Behnia, M., Mills, D., 2003. Modelling of cavity receiver heat transfer for the compact linear Fresnel reflector. In: Presented at the ISES World Congress.

Pye, J.D., 2008, System modelling of the compact linear Fresnel reflector, PhD thesis, University of New South Wales, Australia.

Qiu, Y., He, Y.L., Cheng, Z.D., Wang, K., 2015. Study on optical and thermal performance of a linear Fresnel solar reflector using molten salt as HTF with MCRT and FVM methods. *Appl. Energy* 146, 162-173.

Reynolds, D.J., Jance, M.J., Behnia, M., Morrison, G.L., 2004. An experimental and computational study of the heat loss characteristics of a trapezoidal cavity absorber. *Sol. Energy* 76, 229-234.

Ross, M.J., 2016. How the 1973 oil embargo saved the planet. Available from https://www.foreignaffairs.com/articles/north-america/2013-10-15/how-1973-oil-embargo-saved-planet.

Sahoo, S.S., Singh, P.L., Banerjee, R., 2012. Analysis of heat losses from a trapezoidal cavity used for linear Fresnel reflector system. *Sol. Energy* 86, 1313-1322

Sahoo, S.S., Varghese, S.M., Kumar, C.S., Viswanathan, S.P., Singh, S., Banerjee, R., 2013a. Experimental investigation and computational validation of heat losses from the cavity receiver used in linear Fresnel reflector solar thermal system. *Renew. Energy* 55, 18-23.

Sahoo, S.S., Singh, S., Banerjee, R., 2013b. Steady state hydrothermal analysis of the absorber tubes used in linear Fresnel reflector solar thermal system. *Sol. Energy* 87, 84-95.

Selig, M., Mertins, M., 2010. From saturated to superheated direct solar steam generation – technical challenges and economical benefits. In: Presented at the 16th SolarPACES International Symposium, Perpignan, France.

Sharma, V., Nayak, J.K., Kedare, S.B., 2015. Effects of shading and blocking in linear Fresnel reflector field. *Sol. Energy* 113, 114-138.

Singh, P., Ganesan, S., Yadav, G., 1999. Technical note: performance study of a linear Fresnel concentrating solar device. *Renew. Energy* 18, 409-416.

Singh, P.L., Sarviya, R.M., Bhagoria, J.L., 2010. Heat loss study of trapezoidal cavity absorbers for linear solar concentrating collector, *Energy Convers. Manage.* 51, 329-337.

Solar Energy Generating Systems (SEGS), 2016. Solar energy generation systems, California. Available from https://en.wikipedia.org/wiki/Solar_Energy_Generating_Systems.

Solar One, 2016. The Solar One project. Available from https://en.wikipedia.org/wiki/The_Solar_Project#Solar_One.

Thermal Insulation Association of Southern Africa (TIASA), 2001. Thermal insulation handbook. Pretoria: TIASA.

TPS, 2016. Tube and pipe sizes. Available from http://www.tpsd.de/downloads/allgemein/gen_tube_und_pipes_sizes_6th_edition_18.pdf.

United Nations, 2016a. Kyoto Protocol. Available from https://en.wikipedia.org/wiki/Kyoto_Protocol.

United Nations, 2016b. United Nations Climate Change Conference COP 21. Available from https://en.wikipedia.org/wiki/2015_United_Nations_Climate_Change_Conference.

Zhu, G., Wendelin, T., Wagner, M. J., Kutscher, C., 2014. History, current state, and future of linear Fresnel concentrating solar collectors. *Sol. Energy* 103, 639-652.

6. Supplementary material

6.1. Insulation area

According to Fig. 8, the mathematical formulations for calculating the surrounding insulation area are as follow:

The summation of the side insulation area is:

$$Sideareas = 2 \times b \times h = 2 \times b \times 144 \quad \left[mm^2\right] \tag{27}$$

The top insulation area is:

$$Top\ area = 0.5 \times t \times \left[2 \times \left(332 + 2 * b - \frac{2 \times h}{tan\,\theta} \right) - \frac{2 \times t}{tan\,\delta} \right] \left[mm^2\right] \tag{28}$$

Therefore, the total insulation area is:

$$Total\ area = 2 \times h \times b + 2 \times b \times t - \frac{t^2}{tan\,\delta} + \left(332 - \frac{2 \times h}{tan\,\theta} \right) \times t \quad \left[mm^2\right] \tag{29}$$

By substituting 144 and 51 for *h* and θ, respectively (the results of the optimum cavity in section 4.1) in Eq. (29), the total insulation area would be:

$$Total\ area = 288 \times b + 2 \times b \times t - \frac{t^2}{\tan\delta} + \left(332 - \frac{288}{\tan 51} \right) \times t \quad \left[mm^2\right] \tag{30}$$